IRAQI JOURNAL OF APPLIED PHYSICS

The *Iraqi Journal of Applied Physics (IJAP)* is a peer reviewed journal of high quality devoted to the publication of original research papers from applied physics and their broad range of applications. IJAP publishes quality original research papers, comprehensive review articles, survey articles, book reviews, dissertation abstracts in physics and its applications in the broadest sense. It is intended that the journal may act as an interdisciplinary forum for Physics and its applications. Innovative applications and material that brings together diverse areas of Physics are particularly welcome. Review articles in selected areas are published from time to time. It aims to disseminate knowledge; provide a learned reference in the field; and establish channels of communication between academic and research experts, policy makers and executives in industry, commerce and investment institutions. IJAP is a quarterly specialized periodical dedicated to publishing original papers, letters and reviews in: Applied & Nonlinear Optics, Applied Mechanics & Thermodynamics, Digital & Optical Communications, Electronic Materials & Devices, Laser Physics & Applications, Plasma Physics & Applications, Quantum Physics & Spectroscopy, Semiconductors & Optoelectronics, Solid State Physics & Applications, Alternative and Renewable Energy, and Computers and Networks.

ISSN (Print): 1813-2065, ISSN (Online): 2309-1673, ISSN (Letters): 1999-656X

EDITORIAL BOARD

Editorial Office:
P. O. Box 55259, Baghdad 12001, IRAQ
Website: www.iraqiphysicsjournal.com
Emails: info@iraqiphysicsjournal.com, editor_ijap@yahoo.co.uk, editor@ijaponline.com

ADVISORY BOARD

SPONSORED AND PUBLISHED BY
THE IRAQI SOCIETY FOR ALTERNATIVE AND RENEWABLE ENERGY SOURCES & TECHNIQUES (I.S.A.R.E.S.T.)

IRAQI JOURNAL OF APPLIED PHYSICS

ISSN (Print): 1813-2065, ISSN (Online): 2309-1673, ISSN (Letters): 1999-656X

" INSTRUCTIONS TO AUTHORS "

CONTRIBUTIONS

Contributions to be published in this journal should be original research works, i.e., those not already published or submitted for publication elsewhere, individual papers or letters to editor.
Manuscripts should be submitted to the editor at the mailing address:
Iraqi Journal of Applied Physics, Editorial Board, P. O. Box 55259, Baghdad 12001, IRAQ
Website: www.iraqiphysicsjournal.com
Email: editor@iraqiphysicsjournal.com, editor_ijap@yahoo.co.uk

MANUSCRIPTS

Two hard copies with soft copy on a compact disc (CD) should be submitted to Editor in the following configuration:

- **One-column** Double-spaced one-side A4 size with 2.5 cm margins of all sides
- Times New Roman font (16pt bold for title, 14pt bold for names, 12pt bold for headings, 12pt regular for text)
- Letters should not exceed 10 pages, papers should not exceed 20 pages and reviews are up to author.
- Manuscripts presented in English only are accepted.
- English abstract not exceed 150 words
- 4 keywords (at least) should be maintained on (PACS preferred)
- Author(s) should express all quantities in SI units
- Equations should be written in equation form (*italic* and symbolic)
- Figures and Tables should be separated from text
- Figures and diagrams can be submitted in colors for assessment and they will be returned to authors after provide printable copies
- Charts should be indicated by the software used for
- Only original or high-resolution scanner photos are accepted
- For electronic submission, articles should be formatted with MS-Word software.

AUTHOR NAMES AND AFFILIATIONS

It is IJAP policy that all those who have participated significantly in the technical aspects of a paper be recognized as co-authors or cited in the acknowledgments. In the case of a paper with more than one author, correspondence concerning the paper will be sent to the first author unless staff is advised otherwise.
Author name should consist of first name, middle initial, last name. The author affiliation should consist of the following, as applicable, in the order noted:
- Company or college (with department name or company division), Postal address, City, state, zip code, Country name, contacting telephone, and e-mail

REFERENCES

The references should be brought at the end of the article, and numbered in the order of their appearance in the paper. The reference list should be cited in accordance with the following examples:
[1] X. Ning and M.R. Lovell, "On the Sliding Friction Characteristics of Unidirectional Continuous FRP Composites", *ASME J. Tribol.*, 124(1) (2002) 5-13.
[2] M. Barnes, "Stresses in Solenoids", *J. Appl. Phys.*, 48(5) (2001) 2000–2008.
[3] J. Jones, **"Contact Mechanics"**, Cambridge University Press (Cambridge, UK) (2000), Ch.6, p.56.
[4] Y. Lee, S.A. Korpela and R. Horne, "Structure of Multi-Cellular Natural Convection in a Tall Vertical Annulus", Proc. 7th International Heat Transfer Conference, U. Grigul et al., eds., Hemisphere (Washington DC), 2 (1982) 221–226.
[5] M. Hashish, "Waterjet Technology Development", High Pressure Technology, PVP-Vol. 406 (2000) 135-140.
[6] D.W. Watson, "Thermodynamic Analysis", ASME Paper No. 97-GT-288 (1997).
[7] C.Y. Tung, "Evaporative Heat Transfer in the Contact Line of a Mixture", Ph.D. thesis, Rensselaer Polytechnic Institute, Troy, NY (1982).

PROOFS

Authors will receive proofs of papers and are requested to return one corrected hard copy with a WORD copy on a compact disc (CD). New materials inserted in the original text without Editor permission may cause rejection of paper.

COPYRIGHT FORM

Author(s) will be asked to transfer copyrights of the article to the Journal soon after acceptance of it. This will ensure the widest possible dissemination of information.

OFFPRINTS

Authors will receive offprints free of charge and any additional reprints can be ordered.

SUBSCRIPTION AND ORDERS

Annual fees (4 issues per year) of subscription are:
50 US$ for individuals inside Iraq; **200** US$ for institutions inside Iraq;
100 US$ for individuals abroad; **300** US$ for institutions abroad.
Fees are reduced by 25% for I.S.A.R.E.S.T. members. Orders of issues can be submitted by contacting the editor-in-chief or editorial office at admin@iraqiphysicsjournal.com, or editor_ijap@yahoo.co.uk to maintain the address of issue delivery and payment way.

IRAQI JOURNAL OF APPLIED PHYSICS
Vol. 16, No.4, October-December 2020, pp. 3-11

Solving Laplace Equation for Numerical Treatment of Surface Potential Generated by Laser-Solid Interaction

Noor E. Naji

Branch of Materials Science, School of Applied Sciences, University of Technology, Baghdad, Iraq

In this work, a numerical treatment to solve Laplace equation was presented in order to determine the electric potential generated at the surface of a solid irradiated by laser pulses. This treatment was based on the finite-difference method (FDM) to give the governing partial differential equation for a particular electromagnetic problem. The experimental data required for the numerical treatment were taken from a solid stainless-steel 304 sample irradiated by 1.069 μm Nd:YAG laser pulses with intensity of 12.4 MW/cm^2. The collected results were interpolated as temporal and spatial voltages and they represent the potential over a lateral distance of 9 mm. The treatment has considered two main considerations; charge and hole size. A large change in the potential values appears the interaction zone. This will cause a large electric field. This means that there is a large force acts on the charges leading to a large acceleration and collision and therefore provides good ionization and absorption conditions, which was not considered before. The most important advantage of this method is it can clearly define for the first time the position of the Knudsen layer, which defines the region where the density, velocity and pressure changes dramatically.

Keywords: Laser-produced plasma; Field emission; Thermoionic emission, Laplace equation
Received: 11 October 2020; **Revised**: 18 November 2020; **Accepted**: 25 November 2019

1. Introduction

Electron emission is defined as liberation of free electron from a surface of a substance caused by the external energy transferred to the electrons. The amount of outside energy required by electron to be emitted from the metal surface is known as work function. The work function usually defined in electron volt (eV) unit [1-3].

The additional external energy required by the electron to emit from the metal surface could come from few sources such as heat energy (thermionic emission), electromagnetic radiation (photoemission) and/or an electric field (field emission) [4-6].

Accordingly there are three methods of obtaining electron emission from the metal surface: field emission, photo emission, and thermionic emission [7].

In electron emission, the additional energy required by the electron come in the form of electric field .Very intense electric field is required to produce field emission [8]. Usually a voltage of the order of a million volts per centimeter distance between the emitting surface and the positive conductor is necessary to cause field emission [9,10]. Field emission can be obtained at temperature much lower than required for thermionic emission and therefore it is also sometimes called as cold cathode emission or auto electronic emission [11].

In photo emission, the additional energy come to cathode by photons if the energy from photons is greater than the metal work function the free electron will knock out from the cathode surface [7]. The emitted electron called as photo electron. The amounts of photo electron depend of the light intensity [8].

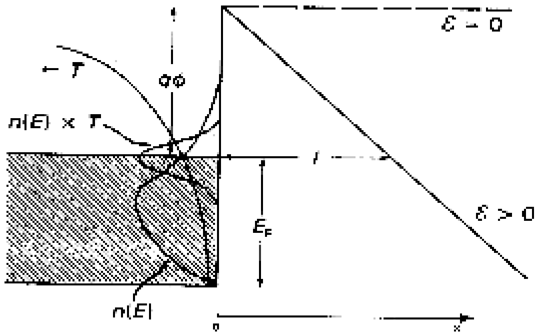

Fig. (1) Free-electron model of a metal surface suitable for the discussion of Field emission process. The tunneling transmission coefficient T increases exponentially with E as the barrier becomes more narrow but the density of occupied states available for tunneling n (E) decreases rapidly above the Fermi energy; the result is that the product of T and n(E) has a maximum near the Fermi energy [4]

Photons illuminating a metal surface may also liberate electrons. If the photon has energy at least equal to the work function, then electrons will be emitted [9], i.e.

$$\lambda < \frac{hc}{e\phi} \qquad (1)$$

where λ is the wavelength of the incident light, c the velocity of light and h Plank's constant.

For shorter wavelengths the electrons are emitted with an initial velocity given by $mv^2=2(hv - e\phi)$ [10].

Photoelectrons are emitted when a single photon (quanta) of energy hv is absorbed by the solid; where h are Planck's constant and v the frequency of the used light [11]. The energy of the photon must be larger than the energy separation between the top of the valence band and the vacuum level. At low temperatures and in metals, this energy is called the work function [12].

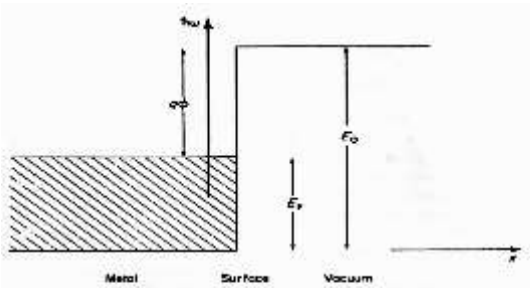

Fig. (2) Free-electron model of a metal surface suitable for the discussion of photoemission processes. When the photon energy *hν* is larger than the work function *qϕ*, photoemission of the photoexcit electron into vacuum is possible [13]

The current density measured at the collecting electrode is given by the fowler equation

$$J = CT^2F\left[\frac{h\nu-e\phi}{k_BT}\right] \qquad (2)$$

where C is nearly a constant and F is a tabulated function that is almost exponential [14]

In the thermoionic method, the additional energy comes to the electron in the form of heat energy, by the electrons the energy transferred into kinetic energy [1]. Thermionic emission is the escape of electrons from a heated surface. Electrons are effectively evaporated from the material. To escape from the metal, electrons must have a component of velocity at right angles to the surface and their corresponding kinetic energy must be at least equal to the work done in passing through the surface [15].

At any finite temperature there is a small fraction of electrons that have a thermal energy higher than the vacuum (Fig. 3) [15].

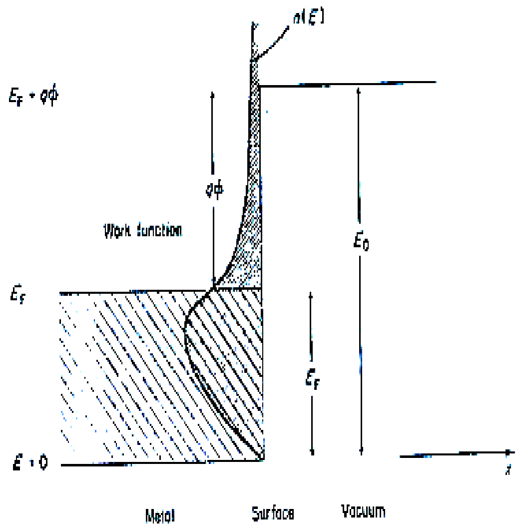

Fig. (3) Free-electron model of a metal surface suitable for the discussion of Thermionic emission processes. Electrons with energy greater than EF+qϕ in the higher energy tail of the Fermi distribution can be emitted into vacuum [12]

The current density can be written as [13]

$$J_{z,th} = AT^2[1+\frac{E_A}{K_bT}]\exp[-\frac{E_w}{K_bT}] \qquad (3)$$

where A is referred to as being the Richardson constant and is given by

$$A = \frac{m^*ek_B^2}{2\pi^2\hbar^3} = \frac{4\pi m^*ek_B^2}{h^3} = 120\,\frac{\mathrm{A}}{\mathrm{cm^2.K^2}} \qquad (4)$$

where m^* is the effective mass, e is the electronic charge, k_B is the Boltzmann constant and h is the Planck's constant [14]

2. Governing Equations

The work is based on Poisson's equation for potential inside the plasma, which can be written as [15]

$$\nabla^2V = -\frac{\rho}{\varepsilon_\circ} \qquad (5)$$

where ∇^2 is the Laplacian operator, V is the potential and ρ is space charge density

In regions of no charges, the equation turns into

$$\nabla^2V = 0 \qquad (6)$$

This equation is called Laplace's equation.

3. Numerical Solution

There are many elegant analytical solutions to Laplace's equation in special geometries, but nowadays, real problems are usually solved numerically [16-20]. Computers and software are now so powerful that it can be easier to obtain a computer solution than to find the exact one in reference books. There are three command methods to finding a numerical solution [21]:

1. Finite-Difference Method (FDM)
2. Finite-Element Method (FEM)
3. Boundary Element Method (BEM)

In our work, the finite-difference method (FDM) is used to give the governing partial differential equation for a particular electromagnetic problem. The steps involved in the application of the FDM are [21,22]:

1) Dividing the domain of interest into a grid (usually rectangular) in one, two or three dimensions as shown below

$V(x,y,z)$ is three dimensional (3D) solution

$V(x,y)$ is two dimensional (2D) solution (no z-variation)

$V(x)$ is one dimensional (1D) solution (no y or z-variation)

2) Developing algebraic equations, which approximate the partial derivatives in the governing equations (difference equations).

3) Solving the set of algebraic equations.

To solve the Poisson's and Laplace's equations numerically, the region of interest can be divided into rectangular grid over which the difference equation approximations to the 2nd order derivatives are defined. The grid points located on the boundaries represent fixed nodes where the potential is known [23,24]. The internal grid points from the boundary are defined as free nodes where the potential must be computed. The grid points are labeled in the x-direction as i, i+1, i+2, etc, and we will label grid point in the y-direction j, j+1, *j*+2, etc. In other words, we will write the equations at all internal nodes of a grid with a regular step size, *h*, in the *x*-direction as Δx, and in the *y*-direction, as Δy as shown in Fig. (4).

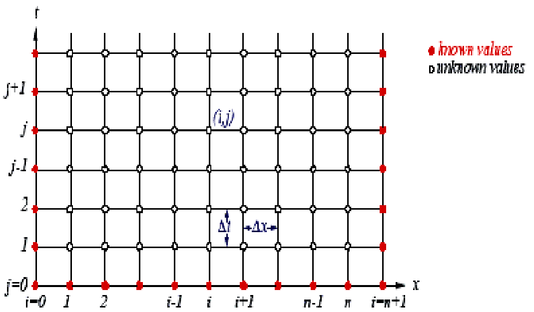

Fig. (4) Two-dimensional grid considered in this analysis, where *i* is spatial index and *j* temporal index

In a source-free region (ρ=0), Poisson's equation is reduced to Laplace's equation

$$\frac{V_{i+1,j}-2V_{i,j}+V_{i-1,j}}{\Delta x^2}+\frac{V_{i,j+1}-2V_{i,j}+V_{i,j-1}}{\Delta y^2}=0 \qquad (7)$$

which is a rectangular-grid 2D Laplace's equation. Also,

$$V_{i,j}\approx\frac{1}{4}[V_{i+1,j}+V_{i-1,j}+V_{i,j+1}+V_{i,j-1}] \qquad (8)$$

which is a square-grid 2D Laplace's equation

The 2D Laplace's equation on a square grid illustrates how the potential at any given point is described as the average of the four surrounding points. Equation (8) could be expressed in matrix from as

AV = B

For solving a discrete PDE, we use the matrix inverse method:

V = A^{-1}B

where *V* is the potential and *A* and *B* are:

$$A=\begin{pmatrix}-4&1&0&1&0&0&0&0&0\\1&-4&1&0&1&0&0&0&0\\0&1&-4&0&0&1&0&0&0\\1&0&0&-4&1&0&1&0&0\\0&1&0&1&-4&1&0&1&0\\0&0&1&0&1&-4&0&0&1\\0&0&0&1&0&0&-4&1&0\\0&0&0&0&1&0&1&-4&1\\0&0&0&0&0&1&0&1&-4\end{pmatrix}\quad B=\begin{pmatrix}B_1\\B_2\\B_3\\B_4\\B_5\\B_6\\B_7\\B_8\\B_9\end{pmatrix}$$

4. Experimental Configuration

A solid stainless steel (St. St. 304) sample was irradiated by Nd:YAG laser pulses with intensity of 12.4 MW/cm^2 and wavelength of 1.069 μm. The laser was focused on spot of area 1.38x10^{-3}cm^2 using a 10cm focusing lens [18]. The laser pulse is shown in Fig. (5), which was detected with optical detector.

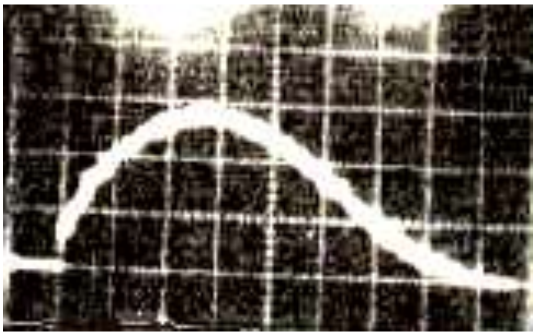

Fig. (5) The Nd:YAG laser pulse considered in this work [25]

A surface voltage is generated during the interaction between laser pulse and the sample and was previously measured [26] as shown in Fig. (6).

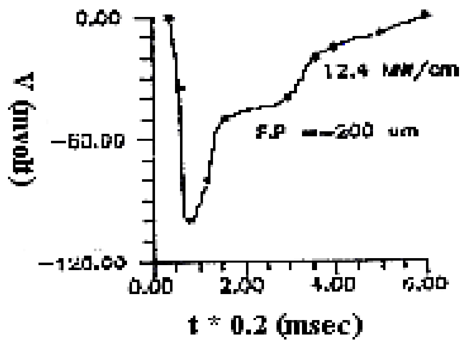

Fig. (6) The voltage generated on a surface irradiated by Nd:YAG Laser pulse as function of irradiation time [26]

A floating potential probe was used at a distance 3mm away from the sample surface to measure the potential of the plasma generated and previously measured [27].

5. Model Assumptions

To start the analytical modeling of the experimental results, it was assumed the following to provide a solution of the problem.

1. Considering the material as a layer that first melts then evaporates, where the skin depth represents thickness of this layer and the spot area represents the area of this layer.
2. The system is placed into an evacuated chamber where the right and left boundary voltages (V_{bR} and V_{bL}) are zero.
3. Neglecting the charge loss produced from attraction of charge with surface.
4. The net charge, not the positive or the negative charge, is considered because the data taken from reference [27] represent the net charge.
5. The ionization by absorption is neglected.
6. No time delay between the charge at the boundary and the interaction zone occurs. This is needed for proper time analysis.
7. The charge is not accumulated at the interaction zone. This is true only for high vacuum.
8. Assume the problem is spatially 3D (*x*,*y*,*z*) and because of symmetry around *z* we have considered

IRAQI JOURNAL OF APPLIED PHYSICS
Vol. 16, No.4, October-December 2020, pp. 3-11

(*x*,*z*) for simplicity and reducing matrix size and time of calculation.

9. The Cartesian coordinates were used because the charge distribution and motion is not a point source or cylindrical.

The considered model needs many predefined parameters as well as numerical solutions of Laplace and Poisson equations. The working steps are:

5.1 Boundary Conditions Consideration

The values of the boundary conditions are taken as: (a) Metal surface potential boundary data values are provided by reference [28], the experimental temporal voltage variation of the surface is shown in Fig. (7). This potential is generated from the reaction of the St-St. 304 sample with the Nd:YAG laser pulses of incident intensity 12.4 MW/cm^2

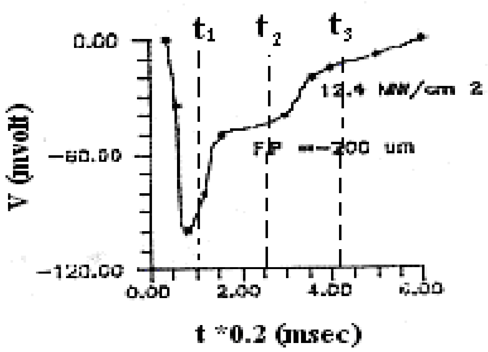

Fig. (7) The instantaneous potential difference measured over time provided by [28]

Using least square fitting (LSF) to represent these results with polynomials yields the results shown in the appendix, where t_1, t_2 and t_3 are selected times on the curve shown in Fig. (7). The data (-) and polynomials (*) are plotted and shown in Fig. (8) and a good agreement is observed.

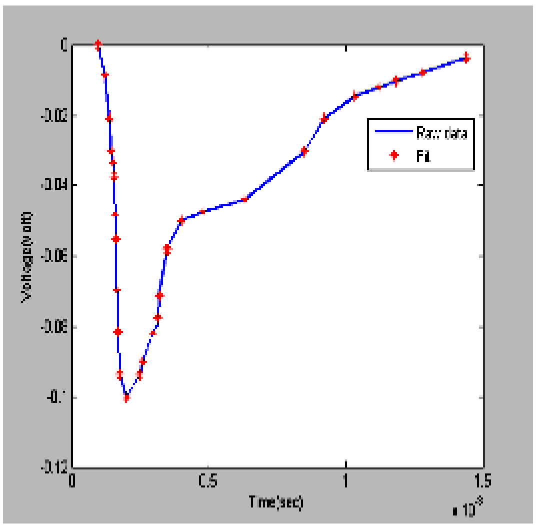

Fig. (8) The representation of the experimental data and curve fitting polynomial of the potential

(b) The boundary data at a distance of 3mm away from the surface is taken from the experimental result of reference [29], which measured the temporal voltage using three floating probes: one single cylindrical and two circular (4.5 and 9 mm in diameter). These results are collected and interpolated as temporal and spatial voltages and they represent the potential over a lateral distance of 9 mm. We can see that in Fig. (9).

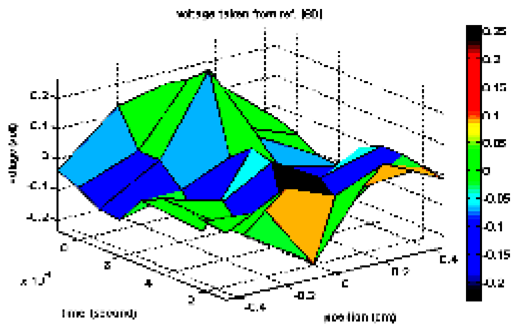

Fig. (9) The temporal variation of voltage at the probes taken from [29]

In this work, the dimensions of the target are 5×2mm^2, therefore, the potentials were selected over a central distance of 5 mm instead of 9 mm and for the same durations, as shown in Fig. (10). They are considered as the upper boundary conditions.

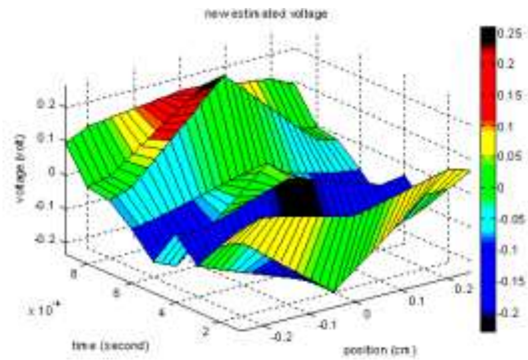

Fig. (10) New estimated voltage at a lateral distance of 5mm

5.2 The Charge Consideration

The values of the charge density were taken from two resources:

First: values obtained from [29] are the values of charge density for different time and space from the center point where the laser interaction with solid as shown in Fig. (11). The data were integrated as:

$$\rho(t) = \int_{x=-4.9}^{4.9} \rho(x,t)dx \qquad (9)$$

The values of $\rho(x,t)$ are taken from all the range in Fig. (12). This charge is assumed to exist in the hole based on the following assumption from charge reservation law:

$$Q_{probe} = Q_{hole}$$

$$\rho_{probe} A_{probe} = \rho_{hole} A_{hole}$$

where ρ_{probe}, ρ_{hole}, and A_{probe}, A_{hole} are charge densities and surface areas of probe and hole, respectively

This charge may be distributed on the first layer of the hole, or overall the layers of the hole. For the first layer

$$\left(\frac{\int \rho_{probe}}{H_{w1st}}\right)(L_{probe} t_{probe}) = \rho_{hole}(hkH_w) \qquad (10a)$$

where H_{w1st} and H_w are the number of points of 1st layer (hole) and one layer, respectively, L and t are the length and thickness of the probe, respectively

For all layers

$$\left(\frac{\int \rho_{probe}}{H_{wall}}\right)(L_{probe} t_{probe}) = \rho_{hole}(hkH_w) \qquad (10b)$$

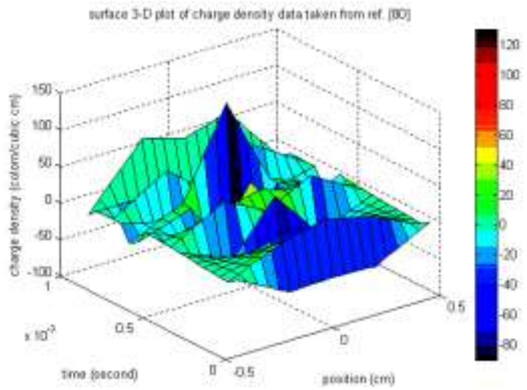

Fig. (11) Surface of 3D plot of charge density data

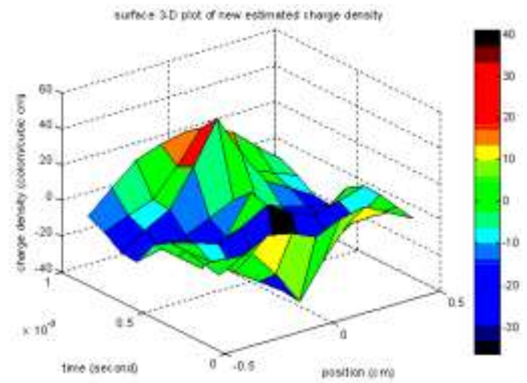

Fig. (12) Surface 3D plot of new estimated charge density

Second: Using thermal emission, we have calculated the total current density as [30]

$J = A^* T^2 \exp(-E_w/k_B T)$ (11)

where A^* is Richardson constant (A/cm^2.K^2), T is the temperature (K), E_w is the work function (J). The electronic current density can be obtained by

$J_e = A^* T^2 \exp(-E_w/k_B T) = 138.936$ A/cm^2

$I = J \times A = 736.365036397\times10^{-3}$ A

$Q = I \times t_{layer} = 3788.64252135\times10^{-9}$ C

The charge appears to be very small compared to that calculated from probe measurements. Therefore, we will use the charge from these probe measurements.

5.3 Hole Size Consideration

1. A fixed hole size of 1x1 mm was considered.
2. A variable hole size was considered. It was taken from previous heat model of reference [31] who considered removing a skin layer according to the deposited variable heat delivered by the laser source. The number of layers is temporally varied and changes as:

$$\frac{\Delta n}{\Delta t} = -9.6938e+024t^6 + 2.6055e+023t^5 - 6.3024e+020t^4 + 6.1694e+017t^3$$

$$-2.9029e+014t^2 + 5.6906e+010t + 30932$$

We have derived the size from the following equation:

Z_H (size of hole) = n_L (number of layers at that time) x Z_L (size of layer)

where Z_L (size of layer) = δ (skin depth) x A (spot area)

the skin depth = 10^{-7} cm, and the spot area = 1.38×10^{-3} cm^2

This is satisfactory if we are looking for the variation of voltage over all space over the surface up to upper boundary.

6. Solution of Potential Equation

The potential over the surface up to the boundary is derived by solving Possion's equation numerically [32]

$$\nabla^2 V = -\frac{\rho}{\varepsilon_\circ} \qquad (12)$$

The 2D Poisson's equation in rectangular coordinates is written as

$$\nabla^2 V = \frac{\partial^2 V}{\partial x^2} + \frac{\partial^2 V}{\partial y^2} = -\frac{\rho}{\varepsilon_\circ} \qquad (13)$$

To solve the Poisson and Laplace equations numerically, the same steps were used as discussed before.

In our case, the nodal grid that is created and used in the derivation of the finite difference equations. A grid is spaced every $5\times10^{-3}/d$ cm along the horizontal and vertical axis to ensure that at least 31 nodes are used in obtaining the potential distribution as shown in Fig. (13).

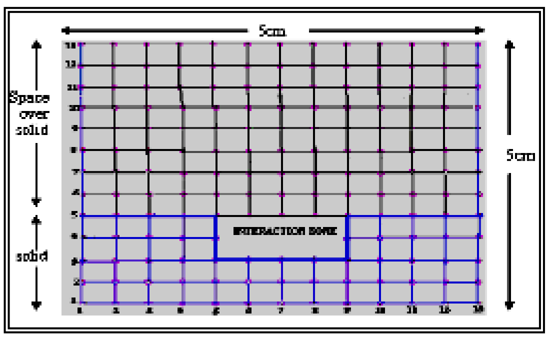

Fig. (13) Nodal grid formed in order to derive the finite difference equations

A 31×31 grid size was used to represent reasonably the actual size 5×5mm and 2mm of the metal surface. Execution of a program with this size of grid is fast since matrix size is not large. Although the program is made flexible to any size, but MATLAB for larger size would be slow.

6.1 Charge consideration

The charges collected on the probes are considered to be the same as in the hole. This is calculated as:

$$Q_{(t)} = \rho_{probe\,(t)}\, L = \rho_{hole\,(t)}\, W \qquad (14)$$

where L is the boundary length, W is the hole length, $\rho_{probe(t)}$ is the temporal charge density on the probe and $\rho_{hole(t)}$ is the temporal charge density in the hole

This charge may be divided equally on the first layer of the hole points or may be divided entirely over all the hole size (2D). The problem is also solved with no charge ($\nabla^2 V$=0) Laplace's equation for comparison.

7. Model Description

Analysis of the plasma potential production from interaction of a laser beam with a workpiece is based on development of a two-dimensional model for the geometry shown in Fig. (14).

The laser beam is characterized by its wavelength λ, the beam spot radius ω_0 at the surface, the skin depth δ, and the power density I within the spot. The workpieces were secured by a rectangular plate with a square hole in the middle, so that the laser beam could irradiate the exposed workpiece in the middle of the clamp plate.

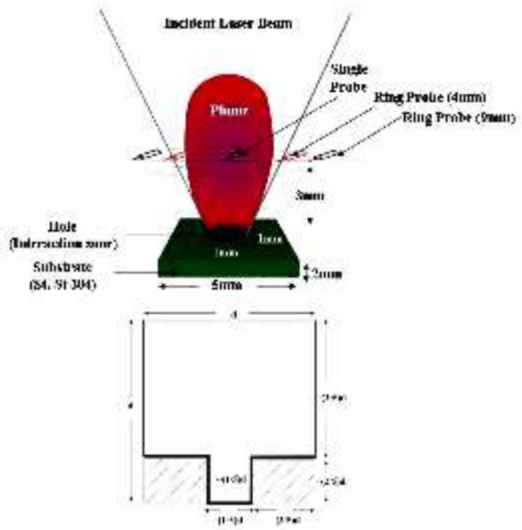

Fig. (14) Schematic description of the boundary conditions of the mathematical model used in this work

The model described in this research to explains a physical matter that can be described as formed of a material (St. St. 304) of 2mm thickness and 5mm length, three probes (single cylindrical, and two ring probes of 9 and 4.5mm diameters) at a distance of 3mm from the target, where the values produced from these probes were assumed as boundary conditions for the upper limits of the model and the boundary condition of the lower limit of the model have been taken from references [33-35]. Finally, the boundary conditions on the left and right side of the mathematical model has been assumed zero considering that the system is located in an evacuated chamber, as shown in Fig. (14). The results have taken into account all the variables mentioned above according to the following diagram.

8. Results and Discussion

The problem is also solved with no charge $\nabla^2 V = 0$ Laplace's equation for comparison. We have solved the problem with not hole and with only metal surface potential boundary data values as shown in Fig. (15).

The problem was solved in the same case as in the case given above over but with metal surface potential boundary data values and with boundary data at 3mm away from the surface as shown in Fig. (16). Also, we have solved the problem with hole but we may consider affixed hole size (1×1mm) and with only metal surface potential boundary data values as shown in Fig. (17).

The problem is solved in the same case as before but with metal surface potential boundary data values and with boundary data at 3mm away from the surface as shown in Fig. (18). We also have solved the problem with hole, and we may consider hole size a variable with time but with only metal surface potential boundary data values as shown in Fig. (19).

We have solved the problem in the same case as before but with metal surface potential boundary data values and with boundary data at 3mm away from the surface as shown in Fig. (20).

By comparing the results, the step in the potential due to boundary condition appears small because of the scale range. The potential Gaussian distribution doesn't appear in Fig. (15). This is clearly demonstrate how importance to consider the potential in the interaction zone. By comparing the results of figures (16 to 20) with the corresponding cases in Fig. (16), they demonstrate the same importance of the existence of the potential.

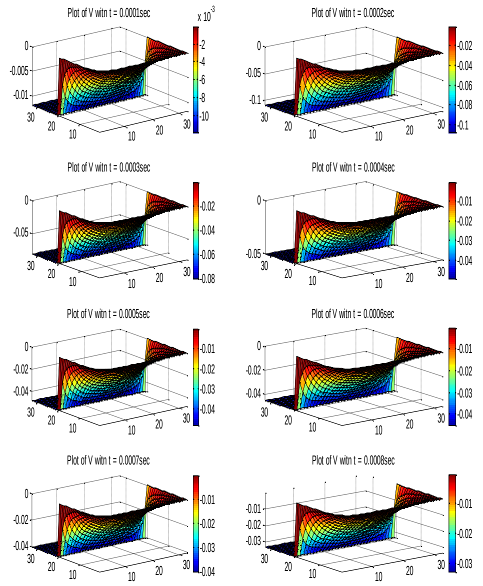

Fig. (15) The solution of the problem with not hole and with only metal surface potential boundary data values

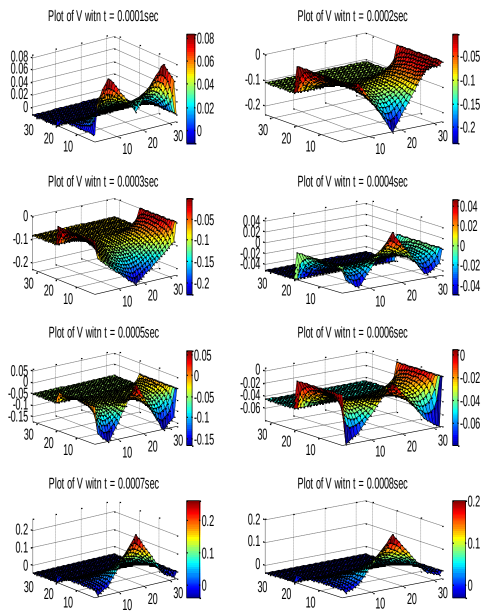

Fig. (16) The solution of the problem in the same case as before of over but with metal surface potential boundary data values and with boundary data at 3mm away from the surface. Boundary data at 3mm away from the surface

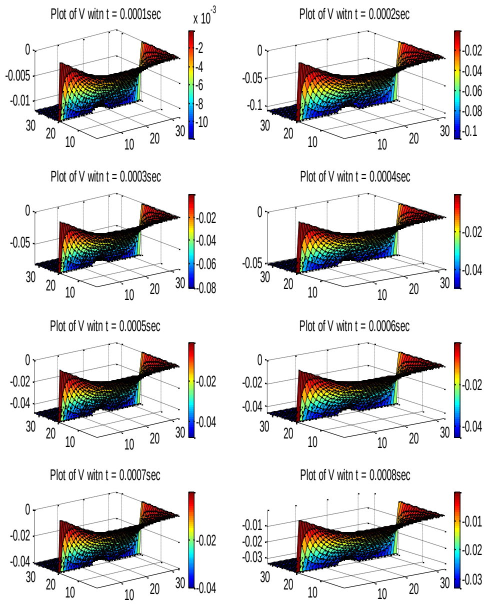

Fig. (17) The solution of the problem with hole but we may consider affixed hole size (1×1mm) and with only metal surface potential boundary data values

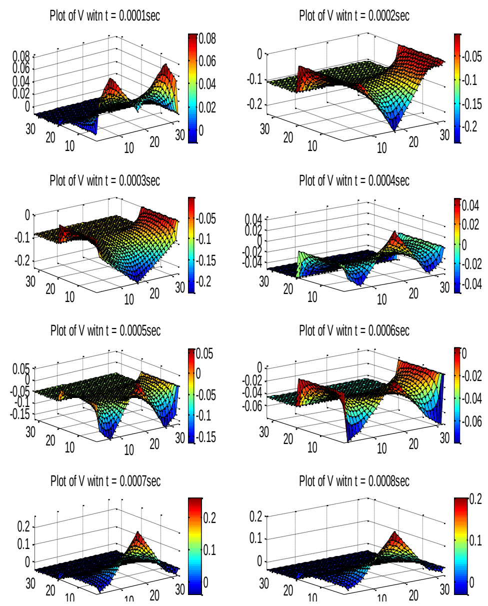

Fig. (18) The solution of the problem in the same case as before but with metal surface potential boundary data values and with boundary data at 3mm away from the surface

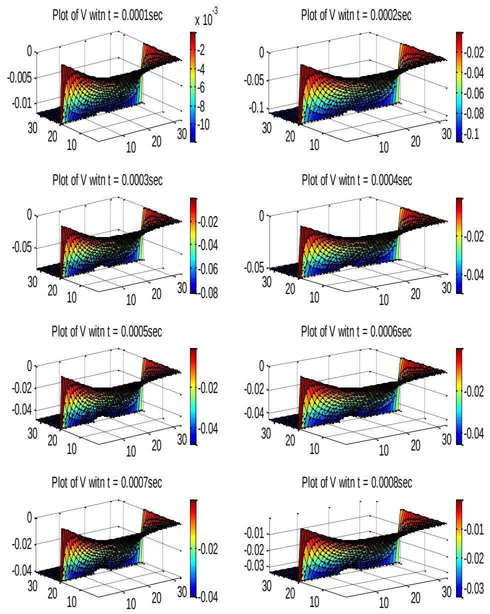

Fig. (19) The solution of the problem with hole, and we may consider a variable hole size with time but with only metal surface potential boundary data values

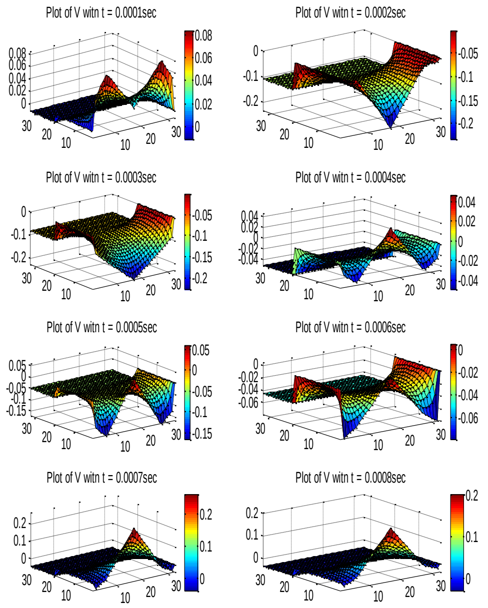

Fig. (20) The solution of the problem in the same case as before but with metal surface potential boundary data values and with boundary data at 3mm away from the surface

9. Conclusions

According to the results obtained from this work, the following remarks can be concluded. A large change in the potential values appears the interaction zone. This will cause a large electric field. This means that there is a large force acts on the charges leading to a large acceleration and collision and therefore provides good ionization and absorption conditions, which was not considered before. The most important advantage of this method is it can clearly define for the first time the position of the Knudsen layer, which defines the region where the density, velocity and pressure changes dramatically. For comparison, we have calculated the potential where boundary voltage, charge and hole are removed. This comparison clearly shows that the potential changes mentioned previously are genuine effect. The amount of the potential gradient depends on the charge. The symmetry of the potential distribution is affected by the boundary condition, while the value of the potential proportional to it.

References

[1] M. Moisan and Z. Zakrzewski, “Plasma sources based on the propagation of electromagnetic surface waves”, *J. Phys. D: Appl. Phys.*, 24 (1991) 1025.

[2] N.R. Isenor, “Effect of background gas on laser-induced electron emission from metal surfaces”, *J. Appl. Phys.*, 36 (1965).

[3] C.M. Verber and A.H. Adelman, “Laser-induced thermoionic emission from tantalum”, *J. Appl. Phys.*, 36 (1965).

[4] P. Langer and G. Tonon, "Laser induced emission of electrons, ions and X-ray from solid targets", *IEEE J. Quantum Electron.*, 2(9) (1966).

[5] T.U. Arifov and G.A. Askarian, "Laser-induced current pulses from a target in a gas", *Sov. Phys. JETP*, 13(2) (1968).

[6] T.U. Arifov and V.A. Makarenko, "Emission of negatively charged particles in laser irradiation of tungsten", *Sov. Phys. JETP*, 21(2) (1976).

[7] T.U. Arifov and V.A Makarenko, "Emission of hot electrons from metals by microsecond laser pulses", *Sov. Phys. JETP*, 23(5) (1978).

[8] J. Teng Lin and T.F. George, "Laser-generated electron emission from surfaces: effect of the pulse shape on temperature and transient phenomena", *J. Appl. Phys.*, 54(1) (1983).

[9] B.I. Vasile'v and A.Z. Grasyuk, "Change in the potential of a charged target subjected to a laser plasma", *Sov. Phys. Tech. Phys.*, 31(5) (1986).

[10] L.A. Gizzi et al., "Measurements of thermal transport in plasmas produced by picosecond laser pulses", *Laser and Particle Beams*, 13(4) (1995) 511-524.

[11] J.R. Ho, C.P. Grigopoulos and J.A.C. Humphrey, "Gas dynamics and radiation heat transfer in the vapor plume produced by pulsed laser irradiation of aluminum", *J. Appl. Phys.*, 79(9) (1996) 7205-7215.

[12] M. Borghesi et al., "Characterization of laser plasmas for interaction studies", *Phys. Rev. E*, 54(6) (1996) 6769-6773.

[13] T. Ditmire et al., "keV x-ray spectroscopy of plasmas produced by the intense picosecond irradiation of a gas of xenon clusters", *J. Phys. B: At. Mol. Opt. Phys.*, 31 (1998) 2825-2831.

[14] V.K. Senecha et al., "Volume effect of laser produced plasma on X-ray emissions", *Pramana J. Phys.*, 55(5-6) (2000) 789-795.

[15] M.I.K. Santala et al., "Effect of the plasma density scale length on the direction of fast electrons in relativistic laser-solid interactions", *Phys. Rev. Lett.*, 84(7) (2000) 1459-1462.

[16] K.W. Ledigham et al., "Photonuclear physics when a multiterawatt laser pulse interacts with solid targets", *Phys. Rev. Lett.*, 84(5) (2000) 899902.

[17] J. Hermann et al., "Investigation of SiO emission spectra observed in a pulsed discharge and a laser-induced plasma", *J. Phys. B: At. Mol. Opt. Phys.*, 34 (2001) 1917-1927.

[18] M. Galemberti et al., "Investigation of ultraintense femtosecond laser-plasma interactions through w and 2w imaging and spectroscopy", *Laser and Particle Beams*, 19 (2001) 47-53.

[19] A. Salcedo et al., "Studies of stimulated Raman scattering in laser plasma interactions", *Private communications*, 2002.

[20] P. Tomassini et al., "Application of novel techniques for interferogram analysis to laser-plasma femtosecond probing", *Laser and Particle Beams*, 20 (2002) 195-199.

[21] M. Borghesi et al., "Electric field detection in laser-plasma interaction experiments via the

proton imaging technique", *Phys. of Plasma*, 9(5) (2002) 2214-2220.
[22] P. Tomassini et al., "Spectroscopy of laser-plasma accelerated electrons: A novel concept based on Thomson scattering", *Phys. of Plasma*, 10(4) (2003) 917-920.
[23] L.A. Gizzi et al., "Transient ionization in plasmas produced by point-like irradiation of solid Al targets", *Phys. of Plasma*, 10(12) (2003) 4601-4604.
[24] M. Borghesi et al., "Measurement of highly transient electrical charging following high-intensity laser-solid interaction", *Appl. Phys. Lett.*, 82(10) (2003) 1529-1531.
[25] T.E. Itinia et al., "Numerical study of ultra-short laser ablation of metals and laser plume dynamics", *Appl. Phys. A: Mater. Sci. Process.*, (2004) 1-4.
[26] S.Q. Al-Qaisy, "Studying the surface charge resulted from plasma generated from its interaction with laser", M.Sc. thesis, 1995, University of Technology, Baghdad.
[27] "Electron Emission", on line report available at http://ww.sap.or.id/.
[28] L.J. Kevin, G.O. Patrick and W.F. Donald, "Generalized electron emission model for field, thermal, and photoemission", *Appl. Phys. Lett.*, 81(20) (2002).
[29] H.B. Richard, **"Electrons in Solids: An Introductory survey",** 2nd ed. 1986.
[30] "Other Important Properties of material", online report available at http://ww.asu.edu/~Ferry/ECE352.htm .
[31] B. Gerold, **"Solid State Physics"**, Int. ed. 1985 by Academic Press, Inc.
[32] M. von Allmen, **"Laser-Materials Processing"**, Springer-Verlag (Berlin), 1996.
[33] B. Eliasson, "Numerical of Vlasov-Maxwell Modeling of Space Plasma", Ph.D. thesis, 2002, Uppsala University, Sweden.
[34] "Numerical Solution of the Transient Diffusion Equation using the Finite Difference Method", online report available at http://www.research.ibm.com/jourrnal/rd/444/jordansweet.html
[35] S.M. Ali, "Laser-Plasma Interaction", M.Sc. thesis, 1992, School of Applied Sciences, University of Technology, Baghdad.

Appendix

$V_1(t)$=8.758231326297914e+023t^6-9.647570877481166e+020t^5+4.3214683770712e+017t^4+1.004569463264522e+014t^3+1.274971036417507e+010t^2-8.371153279949487e+005t+2.221652415436611e+001 *for* $0 \le t \le t_1$

$V_2(t)$=-4.216190398182638e+010t^3+4.106638304623091e+007t^2 -1.283412744333760e+004t+1.211358590639905e+000 *for* $t_1 \le t \le t_2$

$V_3(t)$=1.058336673315529e+00t^2-8.700171524786168e+001t-3.133347479914106e-002 *for* $t_2 \le t \le t_3$


58th Winter Nuclear & Particle
Physics Virtual Conference
WNPPC 2021
February
9-12 2021
WNPPC.TRIUMF.CA
The Winter Nuclear and Particle Physics Conference is a national meeting for the Canadian subatomic physics community, with a special focus on providing a forum for junior researchers (students and postdocs) to present their research and interact with groups across Canada. The 2021 meeting is being organized by McGill University and TRIUMF, and as usual will feature sessions focusing on the research areas of interest to the Canadian subatomic physics community, both experimental and theoretical.
TOPICS
Electroweak and Higgs physics
Neutrino properties
QCD and hadrons
Physics beyond the Standard Model
Nuclear structure
Nuclear and particle astrophysics
ORGANIZING COMMITTEE
Prof. Thomas Brunner (McGill – chair)
Prof. Andreas Warburton (McGill)
Prof. Ken Ragan (McGill)
Prof. Beatrice Franke (TRIUMF)
Prof. Blair Jamieson (University of Winnipeg)
Prof. Gwen Grinyer (University of Regina)
Prof. Alain Bellerive (Carleton University)
Prof. Tony Noble (Queen's University)
Prof. Jens Dilling (TRIUMF)
Jana Thomson (TRIUMF)
McGill
TRIUMF
SNOLAB
MINING FOR KNOWLEDGE
CREUSER POUR TROUVER... L'EXCELLENCE
Canadian Association of Physicists
INSTITUTE OF PARTICLE PHYSICS
CINP
ICPN
PERIMETER INSTITUTE
Arthur B. McDonald
Canadian Astroparticle Physics Research Institute

Ruqia A.H. Hassan
Fuad T. Ibrahim

Department of Physics,
College of Science,
Baghdad University,
Baghdad, IRAQ

Preparation and Characterization of Anatase Titanium Dioxide Nanostructures as Smart and Self-Cleaned Surfaces

Highly-pure titanium dioxide (TiO_2) thin films were prepared by dc reactive magnetron sputtering technique onto glass substrates after different deposition times. The XRD pattern of TiO_2 powders extracted from the thin film samples showed intense and sharp reflections from the crystal planes belonging to the tetragonal anatase phase of TiO_2. As well, scanning electron microscopy has confirmed the formation of smooth and well-dispersed nano-surfaces. The optical measurements in the wavelength range 300-800 nm have confirmed that the energy band gap of the prepared films was ranging in 3.2-3.4 eV. The contact angle measurements were carried out using the sessile drop method as the contact angle of water droplet on the surface was measured before and after irradiation of these surfaces with UV radiation. The results showed that the contact angle of water droplet on the TiO_2 surface decreases after 30 minutes of UV irradiated for all samples, which confirms the high hydropholic characteristics of these samples.

Keywords: Contact angle; Smart surfaces; Self-cleaned surface; Titanium dioxide
Received: 22 October 2020; **Revised**: 20 December 2020; **Accepted**: 27 December 2020

1. Introduction

The development of smart surfaces with switchable wettability have attracted numerous applications including fog-free eyeglasses and windshields, and self-cleaning cloth and glass [1]. With superhydrophilic property, TiO_2 has become one of the most attractive self-cleaning materials in the last two decades [2,3]. Nevertheless, the practicability superhydrophilic of TiO_2 films is limited as the ultraviolet (UV) irradiation is required to create the hydrophilic domains. Furthermore, when UV illumination is switched off, the TiO_2 film loses its superhydrophilic quality within minutes to hours [4]. Hence, the motivation of this work is to develop a TiO_2 film with permanent superhydrophilic wetting and antifogging without need for UV activation [5].

The wetting of a solid with water, where air is the surrounding medium, is dependent on the relation between the interfacial tensions (water/air, water/solid and solid/air). The ratio between these tensions determines the contact angle between a water droplet and a given surface. A contact angle of 0° means complete wetting, and a contact angle of 180° corresponds to complete non-wetting [6]. Hydrophobic surfaces with low wettability and contact angles of about 100° are known for a long time. The higher this angle the lower is the value of the adhesion work. Decreasing of the contact angle leads to enlarged values of the adhesion work (hydrophilic surfaces) [7].

By transferring the microstructure of selected plant surfaces to practical materials, super-hydrophobic surfaces could be developed. The water repellency of plant surfaces has been known for many years. That water-repellent surfaces also indicate self-cleaning properties those been completely overlooked. The correlation between the microstructure, wettability and contaminants in detail using lotus leaves was investigated and proved [8]. This was called the “Lotus Effect” because it can be demonstrated beautifully with the great leaves of the lotus plant. The micro-rough surfaces show contact angles higher than 130° [8]. That means the adhesion of water, as well as particles, is extremely reduced. Water which contacts such surfaces will be immediately contracted to droplets [7]. The particles of contaminants adhere to the droplet surfaces and are removed from the rough surface when the droplets roll of [8].

Different deposition techniques can be used to form titanium oxides films, including plasma-enhanced chemical vapor deposition (PECVD) [9], reactive evaporation [10], spray pyrolysis [11], sol-gel method [12], electron beam evaporation [13], and dc reactive magnetron sputtering [14-16].

This work focuses on preparation of TiO_2 thin films were by dc reactive magnetron sputtering technique. The structural and spectroscopic characteristics of these thin films were studied. In addition, a smart self-cleaning surface was fabricated and characterized from the prepared TiO_2 samples.

2. Experimental work

A homemade dc reactive magnetron sputtering system was used to deposit TiO_2 thin films on glass substrates. The chamber was pumped down by a two-stage Leybold-Heraeuos rotary pump (24 m^3/h) to a base pressure of about $5x10^{-3}$ mbar. The vacuum chamber was cleaned by using glow discharge for five minutes with 10 mA discharge current to remove contaminants on electrodes and inside chamber. Then, the chamber was filled with argon and oxygen gas mixture (1:1) to about $2.5x10^{-1}$ mbar total pressure. A titanium sheet with purity of 99.9% was used as a sputtered target. The discharge current was maintained at 50 mA and the inter-electrode distance was maintained at 4 cm while deposition time was varied (1, 1.5, 2, 2.5 and 3 hours). More details on the dc reactive magnetron sputtering system can be found elsewhere [17-25].

In order to study the structural properties, the crystal structure was analyzed with a Shimadzu 6000 X-ray diffractometer system in which the source of radiation is Cu(kα) with wavelength of 1.5406 Å. A double-beam METERTECH SP8001 UV/Visible spectrophotometer was used to measure the spectroscopic characteristics of the prepared samples in the spectral range of 300- 800nm. The prepared nanostructures were introduced by a JEOL JSM-5600 scanning electron microscope (SEM).

A new technique was used to extract nanopowders from thin films deposited on glass substrates [26,27]. In this technique, the film sample is maintained on a copper plate and cooled down to -20°C using a high-efficiency freezing unit. The sample was then exposed to ultrasonic waves generated by a Triode R.F. Oscillator and two transducers operating in the frequency range of 3-50 MHz.

Hydrophilic behavior was evaluated by measuring the contact angle of a water droplet on the films using contact angle device. A water droplet is injected on the surface of the film using micro-injector (2µl) syringe pointed vertically down onto the sample surface. High resolution camera with macro lens which captures the image of the water droplet, and then analyzed using analysis software.

3. Results and Discussion

As shown in Fig. (1), intense and sharp peaks are seen those belong to the tetragonal crystallography of the anatase phase of TiO_2. All diffraction peaks identified and located at 25.5, 38.1, 48.36, 54.3 and 55.32 are indexed as anatase TiO_2 according to the JCPDS 21-1272 [28]. These peaks correspond to reflections of (101), (004), (200), (105) and (211) planes, respectively. As shown, TiO_2 nanopowder is polycrystalline with preferred orientation in (101) direction. The single phase (anatase) of TiO_2 was produced by preventing the effect of heat during the deposition process of TiO_2 film on the substrate. At temperature of about 600°C, the anatase phase converts into rutile, therefore, the temperature of the substrate placed on the anode surface is reduced by cooling with circulating water at 10°C [29].

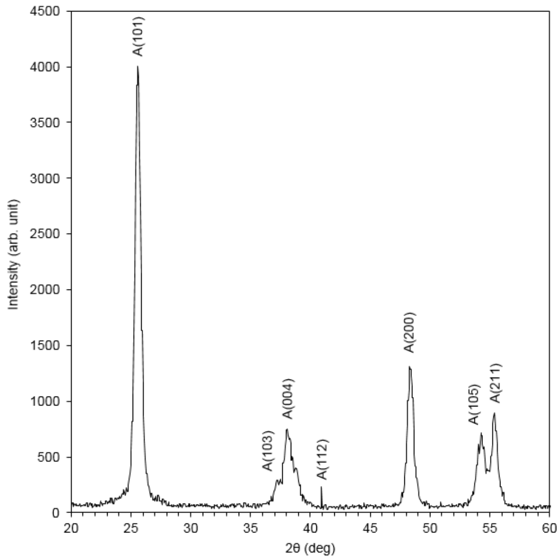

Fig. (1) XRD pattern of TiO_2 nanopowder prepared using 1:1 Ar:O_2 gas mixture after deposition time of 1.5 hours

Figure (2) shows the spectral transmittance of the prepared films in the spectral range of 300-800nm. It is clear that the transmittance is increased with film thickness and all samples shows higher absorption in the UV region and low absorption in the visible region while they are approximately transparent in the near-infrared (NIR) region. Obviously, the absorption edge of TiO_2 thin films lies in the range 360-390nm as the transmittance was rapidly increased in the visible region , which may be attributed to the presence of larger crystallites and hence higher scattering due to the surface roughness [30].

As the film thickness was increased by 100%, the energy band gap was decreased by 0.2 eV (from 3.4 to 3.2 eV). This is necessary to employ these films in some spectroscopic applications requiring thin films to absorb in both UV and visible regions, such as photocatalysts and solar cells. The increase in energy band gap with decreasing film thickness has an effect on the hydrophilic behavior of the prepared samples as this behavior highly depends on the saturation of amount of absorption light.

Table (1) Results of the thickness and energy gap of TiO_2 thin films

Deposition time (hour)	Film thickness (nm)	Energy gap (eV)
1	106.4	3.4
1.5	159.6	3.35
2	190	3.3
2.5	209	3.25
3	212.8	3.2

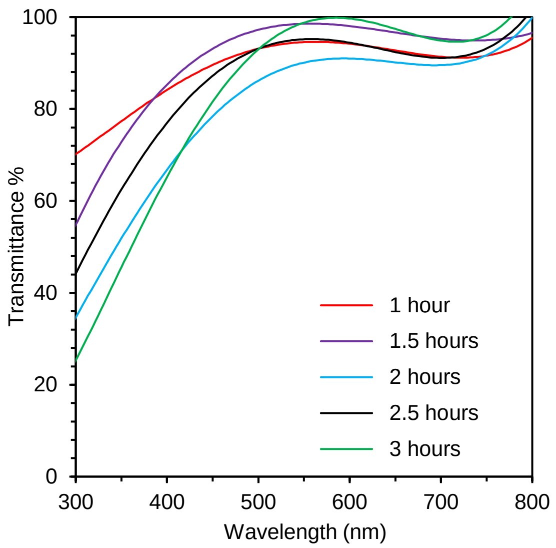

Fig. (2) Transmission spectra of TiO_2 thin films prepared after different deposition times

The FESEM images in Fig. (3) show surface morphology of the TiO_2 thin film sample prepared after deposition time of two hours. Smooth and uniform morphology surface is observed with the presence of granular grains. The nanoparticles show alignment and homogeneous distribution (with no voids), but their diameters are rather uniform. The surface also contains polyhedral shells distributed dispersively on the substrate, with some of them line up along the nanoparticles. These images also show small granular grains distributed throughout the surface without any cracks. The surface is composed of spherical grains of average size 60-80 nm.

The prepared thin films were irradiate with a 18W UV source in the spectral range 200-400nm at an intensity of 10 mW/cm^2 for two different times. The contact angle measurements were performed in air using the sessile drop method. The contact angle of a water droplet was measured on the surface before and after irradiation with UV light for 15 and 30 min.

Figures (4-7) and table (2) shows the results of measuring contact angle of water droplet on the pure TiO_2 surface. Most samples showed that the contact angle was decreased after 15 and 30 min of UV irradiation. The sample prepared after deposition time of 1 hour showed lower thickness and higher surface roughness. This factor has the most effective role on the degree of hydrophilicity. The prepared samples have high hydrophilicity that increased with increasing film thickness. The good super-hydrophilic wetting and antifogging effects were attributed to the highly accessible pores developed on the TiO_2 coated slide, on which the water droplets can be sank. The hydrophilic behavior of the prepared samples depend on the exposure time required by the UV light to reach saturation point.

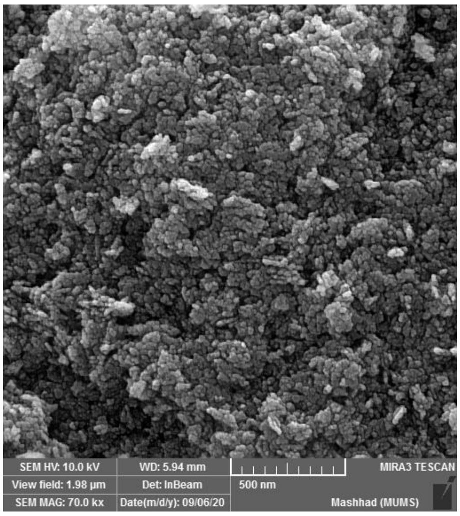

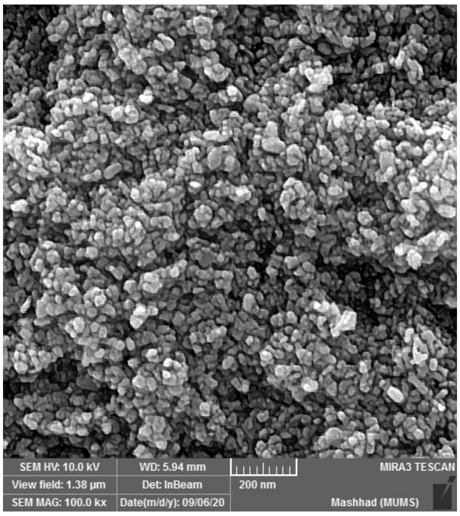

Fig. (3) FESEM images of pure TiO_2 films at two different scales (200 nm and 500 nm)

Table (2) Results of contact angle measurements of TiO_2 samples before and after 15 and 30 min of UV irradiation

Sample	Deposition Time (hour)	Contact angle before exposure to an UV source	Contact angle after exposure to an UV source (15 min)	Contact angle after exposure to an UV source (30 min)
a	1	67.2°	26.05°	16.56°
b	1:30	36.77°	64.78°	9.54°
c	2	80.07°	14.1°	38.16°
d	2:30	32.01°	45.47°	56.09°
e	3	49.19°	9.77°	34.56°

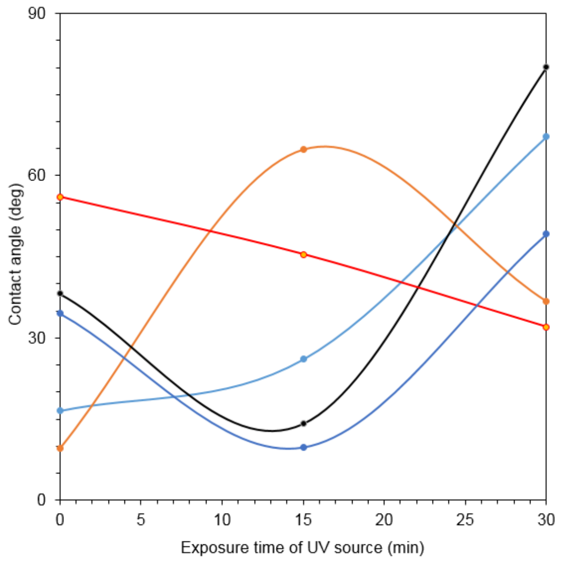

Fig. (4) Contact angles of a pure TiO_2 sample without and with 15 and 30 min. of UV irradiation min

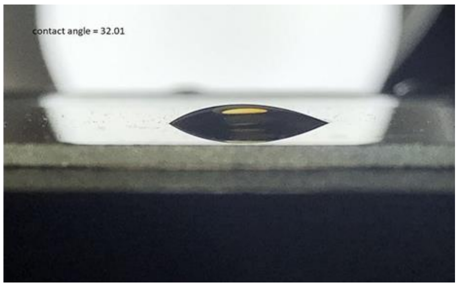

(d)

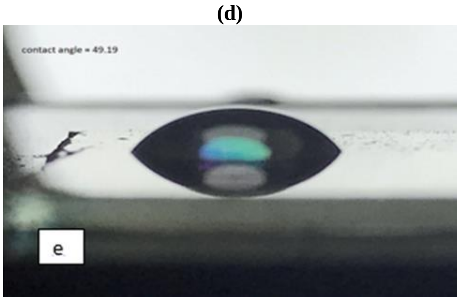

(e)

Fig. (5) Images of water droplet on the TiO_2 surface before irradiation with UV light

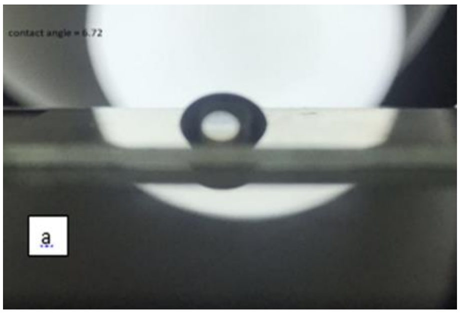

(a)

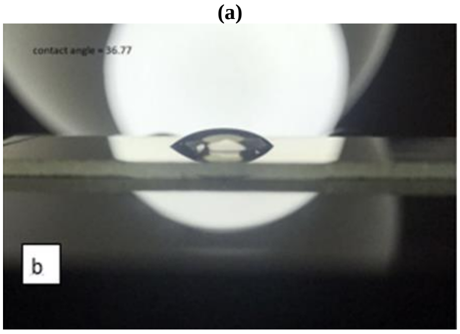

(b)

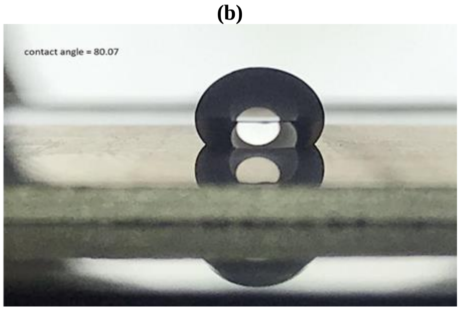

(c)

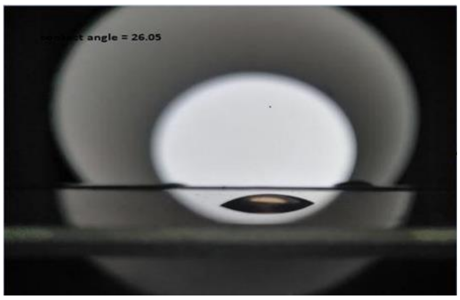

(a)

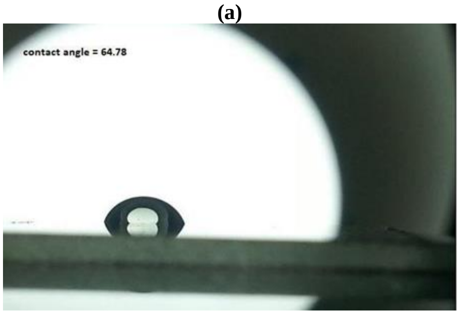

(b)

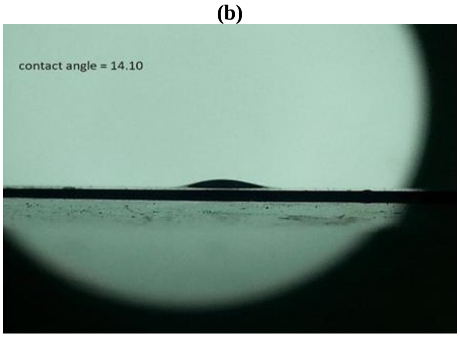

(c)

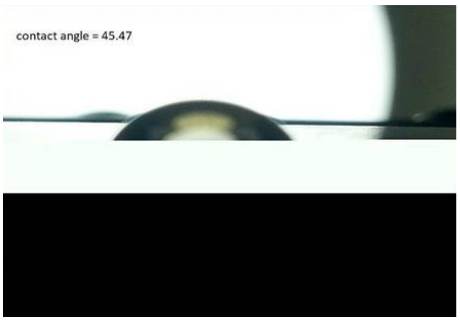

(d)

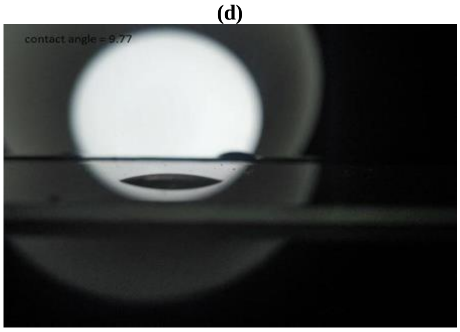

(e)

Fig. (6) Images of water droplet on the TiO_2 surface after 15 min of irradiation with UV light

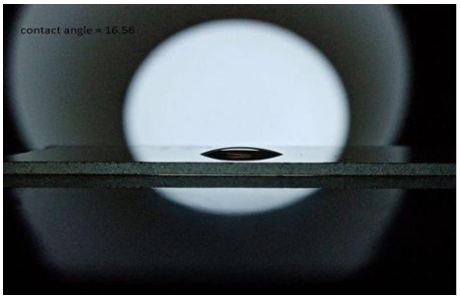

(a)

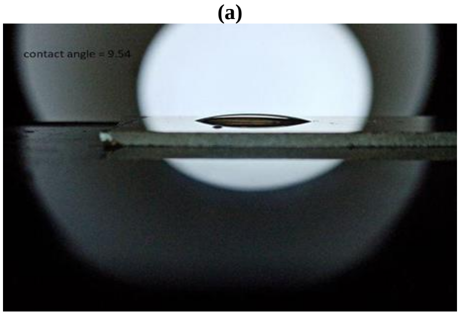

(b)

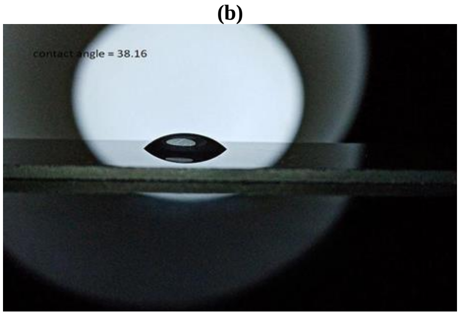

(c)

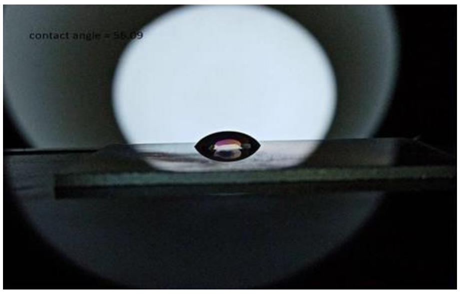

(d)

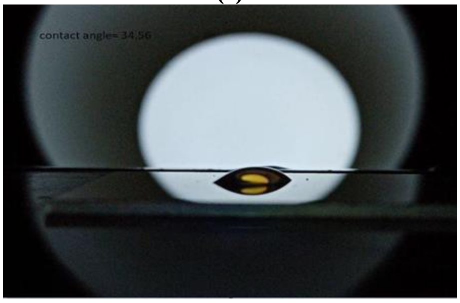

(e)

Fig. (7) Images of water droplet on the TiO_2 surface after 30 min of irradiation with UV light

4. Conclusions

DC reactive magnetron sputtering technique was used as a reliable and flexible technique to prepare highly-pure anatase TiO_2 thin films. The structure of TiO_2 films was tetragonal polycrystalline with a preferred orientation in the (101) direction. Optical measurements showed uniformity and good quality of the prepared films. All prepared samples showed that the contact angle of water droplet on the surface of TiO_2 thin films was decreased after 15 minutes of UV irradiation.

References

[1] K. Hashimoto, H. Irie, and A. Fujishima, “TiO_2 photocatalysis: A historical overview and future prospects”, Japanese J. Appl. Phys., Part 1 Regul. Pap. Short Notes Rev. Pap., 44(12) (2005) 8269–8285.

[2] S.M. Hassan, A.I. Ahmed and M.A. Mannaa, “Preparation and characterization of SnO2 doped TiO_2 nanoparticles: Effect of phase changes on the photocatalytic and catalytic activity”, J. Sci. Adv. Mater. Dev., 4(3) (2019) 400–412.

[3] A. Fujishima, T.N. Rao and D.A. Tryk, “Titanium dioxide photocatalysis,” J. Photochem. Photobiol. C: Photochem. Rev., 1(1) (2000) 1–21.

[4] J. Yu et al., “Preparation and characterization of super-hydrophilic porous TiO_2 coating films”, Mater. Chem. Phys., 68(1–3) (2001) 253–259.

[5] C.C. Chang, Z.M. Lin and L.P. Cheng, “Preparation of organic–inorganic hybridized dual-functional antifog/antireflection coatings on plastic substrates”, J. Appl. Polym. Sci., 137(24) (2020), doi: 10.1002/app.48822.

[6] K.-Y. Law and H. Zhao, “Surface Wetting”, Springer (Switzerland, 2016), p. 142

[7] K.L. Mittal (ed.), “Advances in Contact Angle, Wettability and Adhesion”, vol. 3, Scrivener Publishing (USA, 2018), p. 147, 83.
[8] W. Barthlott and C. Neinhuis, “Purity of the sacred lotus, or escape from contamination in biological surfaces”, Planta, 202(1) (1997) 1-8, 1997.
[9] T. Kamada et al., “Structure and properties of silicon titanium oxide films prepared by plasma-enhanced chemical vapor deposition method”, Japanese J. Appl. Phys., 30(12) (1991) 3594-3596.
[10] M. Grodzicki et al., “Preparation of TiO_2 thin films by reactive evaporation method”, published in 2009 Int. Students and Young Scientists Workshop “Photonics and Microsystems”, pp. 25–27, doi: 10.1109/STYSW.2009.5470308.
[11] L. Castaeda et al., “Spray pyrolysis deposition and characterization of titanium oxide thin films”, Mater. Chem. Phys., 77(3) (2003) 938–944.
[12] S.G. Ullattil and P. Periyat, “Sol-Gel Synthesis of Titanium Dioxide,” Springer, Cham, (2017) pp. 271–283.
[13] H.K. Jang et al., “Titanium oxide films on Si(100) deposited by e-beam evaporation,” J. Vac. Sci. Technol. A: Vac. Surf. Film., 18(6) (2002) 2932-2936.
[14] S.S. Al-Awadi et al., “Optical and structural properties of titanium dioxide papered by dc magneto-sputtering as a NO_2 gas sensor”, Iraqi J. Sci., 61(10) (2020) 2562-2569.
[15] E.A. Al-Oubidy and F.J. Al-Maliki, “Photocatalytic activity of anatase titanium dioxide nanostructures prepared by reactive magnetron sputtering technique”, Opt. Quantum Electron., 51(1) (2019) 23.
[16] E.A. Al-Oubidy and F.J. Al-Maliki, “Effect of Gas Mixing Ratio on Energy Band Gap of Mixed-Phase Titanium Dioxide Nanostructures Prepared by Reactive Magnetron Sputtering Technique”, Iraqi J. Appl. Phys., 14(4) (2018) 19-23.
[17] O.A. Hammadi t al., “Operation Characteristics of a Closed-Field Unbalanced Dual-Magnetrons Plasma Sputtering System”, Bulg. J. Phys., 41(1) (2014) 24-33.
[18] O.A. Hammadi, M.K. Khalaf, F.J. Kadhim, “Fabrication of UV Photodetector from Nickel Oxide Nanoparticles Deposited on Silicon Substrate by Closed-Field Unbalanced Dual Magnetron Sputtering Techniques”, Opt. Quantum Electron., 47(12) (2015) 3805-3813.
[19] O.A. Hammadi, M.K. Khalaf, F.J. Kadhim, “Silicon Nitride Nanostructures Prepared by Reactive Sputtering Using Closed-Field Unbalanced Dual Magnetrons”, Proc. IMechE, Part L, J. Mater.: Design and Applications, 231(5) (2017) 479-487.
[20] O.A. Hammadi, M.K. Khalaf, F.J. Kadhim, “Fabrication and Characterization of UV Photodetectors Based on Silicon Nitride Nanostructures Prepared by Magnetron Sputtering”, Proc. IMechE, Part N, J. Nanoeng. Nanosys., 230(1) (2016) 32-36.
[21] M.A. Hameed and Z.M. Jabbar, “Optimization of Preparation Conditions to Control Structural Characteristics of Silicon Dioxide Nanostructures Prepared by Magnetron Plasma Sputtering”, Silicon, 10(4) (2018) 1411-1418.
[22] O.A. Hammadi and N.E. Naji, “Characterization of Polycrystalline Nickel Cobaltite Nanostructures Prepared by DC Plasma Magnetron Co-Sputtering for Gas Sensing Applications”, Photon. Sens., 8(1) (2018) 43-47.
[23] F.J. Al-Maliki and E.A. Al-Oubidy, “Effect of gas mixing ratio on structural characteristics of titanium dioxide nanostructures synthesized by DC reactive magnetron sputtering”, Physica B: Cond. Matter, 555, 18-20 (2019).
[24] F.J. Al-Maliki, O.A. Hammadi and E.A. Al-Oubidy, “Optimization of Rutile/Anatase Ratio in Titanium Dioxide Nanostructures prepared by DC Magnetron Sputtering Technique”, Iraqi J. Sci., 60 (2019) 91-98.
[25] O.A. Hammadi, F.J. Al-Maliki and E.A. Al-Oubidy, “Photocatalytic Activity of Nitrogen-Doped Titanium Dioxide Nanostructures Synthesized by DC Reactive Magnetron Sputtering Technique”, Nonlinear Opt. Quantum Opt., 51(1-2) (2019) 67-78.
[26] O.A. Hammadi, “Production of Nanopowders from Physical Vapor Deposited Films on Nonmetallic Substrates by Conjunctional Freezing-Assisted Ultrasonic Extraction Method”, Proc. IMechE, Part N, J. Nanomater. Nanoeng. Nanosys., 232(4), 135-140 (2018).
[27] O.A. Hammadi, “Effects of Extraction Parameters on Particle Size of Titanium Dioxide Nanopowders Prepared by Physical Vapor Deposition Technique”, Plasmonics, 15 (2020),DOI: 10.1007/s11468-020-01205-8
[28] M.I. Pratheepa and M. Lawrence, “X-Ray Diffraction Analyses of Titanium Dioxide Nanoparticles”, Int. J. Sci. Res. Sci. Technol., 3(11) (2017) 83-88.
[29] T.R. Esch, I. Gadaczek and T. Bredow, “Surface structures and thermodynamics of low-index of rutile, brookite and anatase - A comparative DFT study”, Appl. Surf. Sci., 288 (2014) 275-287.
[30] B. Soediono, “Enhanced Performance and Functionality of Titanium Dioxide Papermaking Pigments with Controlled Morphology and Surface Coating”, J. Chem. Inf. Model., 53(8) (1989) 160.

IRAQI JOURNAL OF APPLIED PHYSICS
Vol. 16, No.4, October-December 2020, pp. 19-23

Simulation Study on Current Gain Improvement at High Collector Current Densities for CuO/TiO_2 Heterostructure Transistors

Ahmed S. Falah
Khalid R. Jasim

*Department of Electrical Engineering,
College of Engineering,
Al-Mustansiriya University,
Baghdad, IRAQ*

An NPN Si/SiGe/SiGe Graded Heterojunction Bipolar Transistor (SiGe GHBT) has been compared with contemporary NPN Si/SiGe/Si Double Heterojunction Bipolar Transistor (SiGe DHBT) for current gain performance at high collector current densities, using a 2-dimensional MEDICI device simulator. The analysis predicts that the base-collector homojunction of the SiGe GHBT structure is responsible for improved current gain at high collector current density in comparison with the conventional SiGe DHBT and provides the option of operation at higher collector current densities.

Keywords: SiGe GHBT; Current gain; Retarding potential barrier; Linear tapering
Received: 11 July 2020; **Revised:** 25 September 2020; **Accepted:** 1 October 2020

1. Introduction

Silicon-Germanium (SiGe) technology provides the option of bandgap engineering along with the compatibility with the present day Si process technology and hence provides the option of integrating the SiGe technology for advancement of present day device field. Extremely high cut-off frequency of 30 GHz and maximum frequency of oscillation of 50 GHz in the Si/SiGe/Si NPN double heterojunction bipolar transistors (DHBTs) had already been reported for use in mobile communication applications [1]. One important aspect of operation of SiGe devices is their requirement of operation at high current densities to achieve high cut-off frequency performance. Moreover, the scaling down of present day electronic devices forces the operation of these devices at very high collector current densities ($>10^5$ Amp/cm^2). Therefore, the operation and performance of SiGe heterostructure transistors at high collector current densities is of prime concern for the microelectronics researchers and process engineers [2].

It has been already reported that the NPN Si/SiGe/Si DHBT structures exhibit rapid fall in the current gain at high collector current densities [3]. This rapid fall in the current gain leads to the fall in transistor efficiency and make it impractical for use at high collector current densities. The degraded current gain at high collector current densities in DHBT structures is attributed to the formation of retarding potential barrier for electrons at base-collector junction [4]. The velocity saturation of electrons in collector and the valence band offset for holes at base-collector junction leads to the formation of retarding potential barrier. The analysis of NPN Si/SiGe/Si DHBT structure by Cottrel and Yu [3] shows the drop in the collector current density curve as the forward base-emitter bias exceeds approx. 0.77 volts, predicting a sharp fall off in current gain of the transistor above 0.77 volts. Therefore, some alternate HBT structures without valence band offset for holes at base-collector junction need to be evolved for improving the transistor current gain and efficiency at high collector currents [1].

In the present work, the conventional NPN SiGe DHBT structure with uniform 20 *at%* of Ge in base is simulated to supplement the earlier reported results on the formation of retarding potential barrier. These results are used as the basis for comparing the structures evolved to improve the current gain at high current densities. The objective has been to transform the base-collector heterojunction with the closest approximation to homojunction. Therefore, in the present work the GHBT structure with a uniform Ge *at%* in base region and a linearly graded germanium *at%* in collector has been chosen with a perfect homojunction at base-collector metallurgical junction [4]. The base-collector homojunction completely inhibits the formation of retarding potential barrier due to valence band offset and the grading of germanium ensures the strained behavior and stability of the SiGe layers [5]. A further advantage of choosing the NPN GHBT structure lies in the fact that the process of growing a box-type uniform SiGe base layer over a linearly graded SiGe collector region is more practical to achieve dislocation free strained base and collector SiGe layers [4].

A two-dimensional MEDICI device simulator, known for its authenticated results at the device level for SiGe HBT structures [6,7], has been used in the present analysis and the high doping and electric field models have been included. The performance of both the HBT structures for current gain is compared and authenticated by investigating the conduction band electron energy, net carrier concentration profiles, metallurgical junction, and dependence of collector current density on base-emitter bias voltage. A theoretical formulation has been provided to supplement the improved performance obtained in the proposed Si/SiGe/SiGe heterostructure in comparison with SiGe DHBT structure.

2. Theory

In NPN silicon BJT the finite electron concentration n_c in collector-base space charge layer is necessary to sustain the flow of collector current in the transistor. An expression relating the electron density n_c with the collector current density J_c for the constant drift velocity v_{dsat} condition is given as [8]:

$$J_c = qv_{dsat}n_c \tag{1}$$

At sufficiently high collector current density the high electron concentration in the space charge region of collector lowers the potential barrier at base-collector junction. This leads to the onset of Kirk phenomenon [8,9] where the base-collector junction shifts into the collector space-charge region resulting in the vertical widening of the effective neutral base region width. The total voltage across base-collector junction (V_{bctot}) is the sum of built in potential barrier at base-collector junction (V_{bi}) and the terminal base-collector voltage (V_{bct}). At the onset of Kirk phenomenon, (at Kirk current density J_k), the electron density in base-collector space charge region, n_c (= n_k, electron density at start of Kirk effect), is related with the device parameters and V_{bctot} by the expression:

$$n_c = N_c + \left\{ \left((2\varepsilon) \frac{V_{bctot}}{qW_c^2} \right) \right\} \tag{2}$$

where N_c is the collector-doping concentration, ε is the dielectric constant for Si, q is the electronic charge and W_c is the collector width as now whole collector width corresponds to space charge region.

In Si BJT, at the onset of Kirk phenomenon, holes are injected into the collector from the base to compensate the electron charge in collector, resulting in the formation of the current induced base. However, for SiGe DHBTs having a sizable alloy mole fraction, there is a valence band discontinuity for holes at base-collector junction. This valence band discontinuity suppresses the hole injection into the collector as n_c exceeds n_k. Eventually, there will be an accumulation of mobile electrons in collector due to velocity saturation and an accumulation of holes in base due to valence band offset at base-collector junction. The combination of these mobile electrons together with localized holes form a dipole layer and in turn give rise to an electric field E_0. A further increase in the collector current density will consequently increase the dipole strength and increases the electric field E_0. The presence of the electric field E_0 at base-collector heterojunction gives rise to a retarding potential barrier (V_{bp}) in conduction band, which would oppose the electrons flowing from emitter to collector through base. An increased electron density in the base at base-collector junction $n_{(Wb)}$ is now required to support and maintain the electron density n_c and collector current density J_c. The electron density n_c in base-collector space charge region for collector density J_c, in SiGe DHBT derived from the basic Poisson's equation is:

$$n_c = N_c + \left\{ \left((2\varepsilon) \frac{V_{bctot} + E_0 W_c}{qW_c^2} \right) \right\} \tag{3}$$

The electron density in base at base-collector junction $n_{(Wb)}$ required to maintain the n_c inside base-collector space charge region is simply given by using current continuity and Boltzmann statistics across the retarding potential barrier V_{bp} :

$$n_{(Wb)} = n_c \exp\left(\frac{qV_{bp}}{KT} \right) \tag{4}$$

where $KT/q = V_T$ is the thermal voltage

The retarding potential barrier V_{bp} for electrons can be expressed as:

$$V_{bp} = \Delta E_v + KT \ln\left[\frac{J_c}{qv_{dsat}N_b} - \frac{N_c}{N_b} - \frac{2\varepsilon(V_{bctot})}{qN_bW_c^2} \right] \tag{5}$$

where ΔE_v is the valence band discontinuity for holes and N_b is the neutral base width.

Solving Eq. (3), (4) and (5) for a uniformly doped base gives the effect of bias dependent retarding potential barrier V_{bp} and base-emitter biasing V_{be} on the collector current density J_c as:

$$J_c = \left[\left(\frac{qD_n n_{io}^2}{W_b N_b} \right) \left(\frac{e^{\left(\left(qV_{be} + \Delta E_v - V_{bp} \right) / KT \right)}}{1 + \frac{D_n e^{\left(V_{bp} / KT \right)}}{W_b v_{dsat}}} \right) \right] \tag{6}$$

where, n_{i0} is the intrinsic carrier concentration. The modified value of electron density in base at emitter-base junction $n_{(0)}$ in term of V_{bp} is expressed as:

$$n_{(0)} = \left[\left(n_c \left(v_{dsat} W_b \right) \right) + \left(n_c \exp\left(\frac{qV_{bp}}{KT} \right) \right) \right] \tag{7}$$

where [n_c (v_{dsat} W_b) / D_{nb}] is the electron density in the base at the base-emitter junction corresponding to the electron density in base-collector space-charge region n_c

The second term in Eq. (7), [$n_c \{exp\ (qV_{bp}/KT)\}$] is the electron density in base at the base-emitter junction as a result of increased electron concentration in base at base-collector junction because of the retarding potential barrier at base-collector junction.

The relation of the effective band offset δE_v and valence band discontinuity ΔE_v with $n_{(0)}$ and V_{be} (for a specific J_c) is expressed as:

$$V_{be} = \begin{bmatrix} V_t \ln\left\{\left(\frac{n_{(0)}^2}{n_{i0}^2}\right) + \left(\frac{n_{(0)}N_b}{n_{i0}^2}\right)\right\} \\ -\frac{\delta(E_v)}{q} \end{bmatrix} \quad (8)$$

The substitution of the expression for $n_{(0)}$ from the Eq. (7) in Eq. (8) predicts the necessity for an increase in V_{be} to account for the increase in $n_{(0)}$ required to sustain the collector current density J_c. This requirement of increase in V_{be} for a given collector current density J_c will be reflected as a fall in the current gain of the DHBT structure. This prediction is consistent with the discussion of Eq. (6) where an increase in retarding potential barrier V_{bp} at high collector current density predicts a fall in the DHBT collector current density J_c and current gain.

The analysis of SiGe DHBT illustrates the formation of retarding potential barrier at base-collector junction due to valence band offset for holes. The theory also predicts a fall in the current gain at high collector current density as a consequence of this retarding potential V_{bp}. Whereas, the proposed GHBT structure with uniform Ge profile in base and grading of Ge *at%* in collector avoids the retarding potential barrier for electrons at base collector homojunction. Consequently, this structure promises an improved current gain at high collector current density in comparison with SiGe DHBT structure.

3. Simulation Results for SiGe DHBT and GHBT Structures

The current gain performance of the NPN Si/SiGe/Si DHBT and proposed NPN Si/SiGe/SiGe heterostructure is compared for identical device dimensions, doping densities and bias conditions. The surface emitter doping of 5 × 10^{19} cm^{-3} and its thickness W_{e1} of 0.2 μm is chosen to provide ohmic contact. The emitter doping of 1× 10^{19} cm^{-3} and its thickness W_{e2} of 0.1 μm is selected to lower the emitter-base. The base thickness W_b of 0.05 μm with a uniform base doping of 8 × 10^{18} cm^{-3} is chosen in both the structures. The collector doping of 1 × 10^{17} cm^{-3} and thickness W_c of 0.45 μm have been chosen in both the structures.

The germanium profile in different regions of Si/SiGe/Si DHBT and Si/SiGe/SiGe HBT structures is shown in Fig 1. An optimized mole fraction of germanium has been chosen to retain the strained behavior and stability of SiGe regions [5]. A uniform 20 *at%* Ge has been chosen in the base of conventional Si/SiGe/Si *Double* HBT (DHBT) structure, whereas its collector does not contain any germanium mole fraction. The base-collector homojunction, in the proposed Si/SiGe/SiGe *Graded* HBT (GHBT) structure has been ensured by choosing a uniform 20 *at%* Ge in base and tapering it linearly to zero *at%* Ge at the collector ohmic contact.

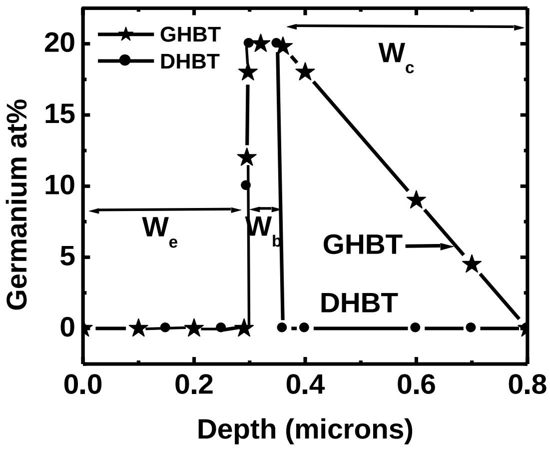

Fig. (1) Ge profile in the emitter, base and collector for the SiGe DHBT and GHBT. W_e, W_b, and W_c are the total emitter, base, and collector width, respectively in the HBTs.

The chosen operating conditions of SiGe DHBT and GHBT structure ensures the performance evaluation in the high collector current density region (>10^5 Amp/cm^2). The simulation results on conduction band electron energy for both the structures include the influence of valence band offset for holes and bandgap narrowing due to the heavily doped base. The electron energy profile shown in Fig. 2, for the collector current density of 9.22 × 10^5 A-cm^{-2}, predict the total retarding potential barrier V_{bp} of approx. 0.09 eV for the conduction band electrons at the base-collector heterojunction in the SiGe DHBT structure. The valence band offset for holes at base-collector heterojunction is observed to contribute 0.06 eV in the total retarding potential barrier in the DHBT structure. This is obtained by excluding the influence of heavy doping effect on band gap narrowing in the base. The simulated result is consistent with the retarding potential barrier of approx. 0.058 eV obtained by solving Eq. (5) for SiGe DHBT accounting only for the valence band offset for holes. Whereas, the formation of such a retarding potential barrier (due to valence band offset for holes) is prohibited by the base-collector homojunction in the GHBT structure. Therefore the simulation results shown in Fig. 2, for the collector current density of 1.6×10^6 A-cm^{-2} in the GHBT structure, exhibits a small potential barrier of 0.03 eV, which is solely attributed to the high doping in the base. The retarding potential barrier of 0.06 eV in the DHBT structure leads to accumulation of mobile electrons at base-collector heterojunction.

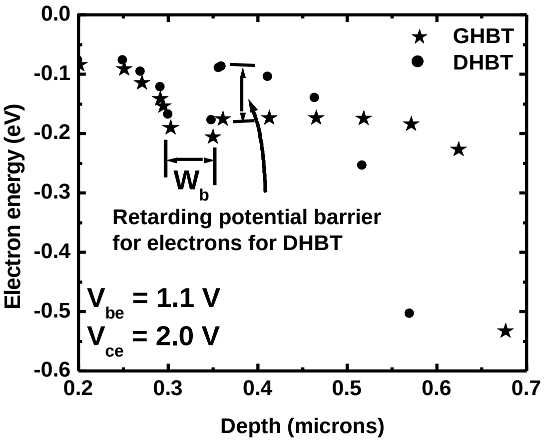

Fig. (2) Conduction band electron energy E_C for SiGe DHBT and GHBT including the effect of valence band offset and band gap narrowing. W_b is the base width

The variation of net carrier concentration with the vertical depth of the SiGe DHBT and SiGe GHBT structures for the chosen bias conditions is shown in Fig. 3. A net carrier concentration of 8.11 $\times 10^{19}$ and 3.93×10^{19} cm^{-3} is obtained in the base of DHBT structure at emitter-base and base-collector junctions, respectively. This corresponds to an electron concentration of 4.36×10^{19} cm^{-3} and 2.92 $\times 10^{19}$ cm^{-3} in the base of DHBT structure at the corresponding metallurgical junctions. Whereas, a lower net carrier concentration of 6.34×10^{18} cm^{-3}, which corresponds to an electron concentration of 1.86×10^{19} cm^{-3}, is obtained, for a higher collector current density of 1.6×10^6 A-cm^{-2} at base-collector junction in the base of GHBT structure. The simulation results predict an electron concentration of 3.07×10^{19} cm^{-3} at the emitter-base junction in GHBT structure.

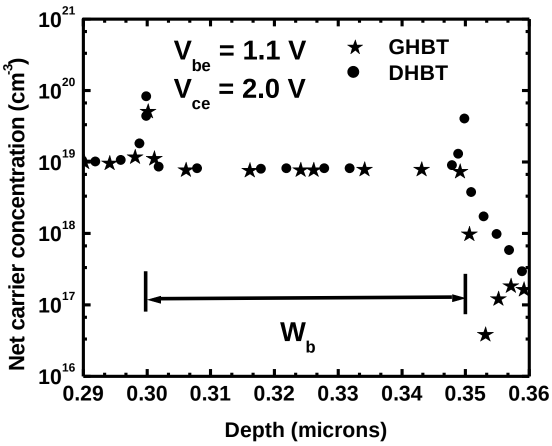

Fig. (3) Net carrier concentration in SiGe DHBT and GHBT at collector-emitter voltage V_{ce} of 2 Volts and base-emitter voltage V_{be} of 1.1 Volts. W_b is the base width

This increase in electron concentration at both the metallurgical junctions in the base of DHBT forces the requirement of an associated increase in base-emitter biasing voltage V_{be}.

The dependence of collector current density J_c on the base-emitter bias voltage V_{be}, for the DHBT and GHBT structures, is shown in Fig. 4. The results predict the requirement of base-emitter bias voltage of 1.1 volts for the DHBT and 0.97 volts for the GHBT structure to sustain the collector current density of 9.22×10^5 A-cm^{-2}. The base-emitter bias voltage for the GHBT structure is observed to increase linearly with the collector current density. Whereas, the collector current density for the DHBT structure approximately saturates above the base-emitter bias voltage of 0.98 volt. Therefore, at higher collector current densities the DHBT structure needs higher base-emitter bias voltage in comparison with GHBT structure, for sustaining the same collector current density, which will adversely influence the current gain of DHBT in comparison with GHBT structure.

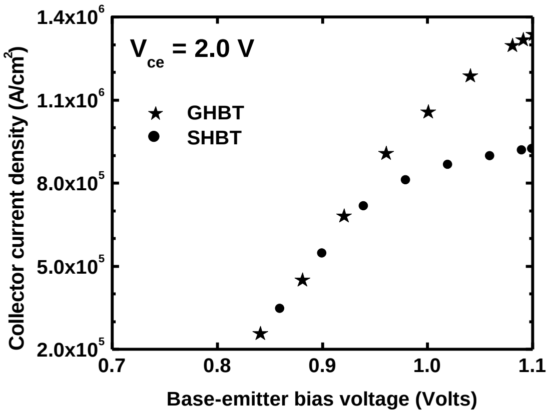

Fig. (4) Dependence of collector current density J_c on base-emitter bias voltage V_{be}

The dependence of current gain on the collector current density for the DHBT and the GHBT structure is shown in Fig. 5. The monotonically decaying behavior of current gain in both the structures for the collector current densities less than 4.0 x 10^5 A/cm^2 is attributed to the Kirk effect [5] and high-level injection of minority carriers in the base. At higher collector current densities (>4.0 x 10^5 A/cm^2), the current gain in the GHBT structure falls to 72% of its initial value for twofold change in the current density. Whereas, the current gain in the DHBT structure falls to 10% for twofold change in the collector current density. Therefore, the DHBT shows a sharp fall-off in the current gain in comparison with GHBT structure as the collector current density increases. The results are consistent with fall in the current gain in DHBT structure, predicted by Eq. (6), due to the formation of retarding potential barrier at base-collector junction in the DHBT structure. The results establish superior current gain performance of the GHBT structure in comparison with the DHBT device. Although the results presented in the present work are for the pre-selected doping profiles and physical parameters of the device but the phenomena of better performance of the GHBT structure over contemporary DHBT structures will be consistent with other device configurations and doping profiles.

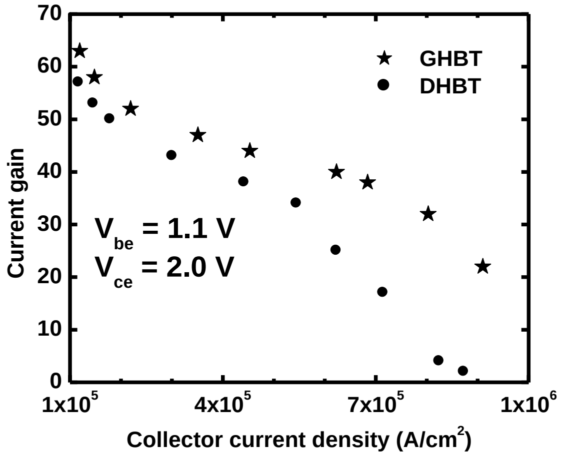

Fig. (5) Current gain Vs. collector current density plot for NPN SiGe DHBT and GHBT

4. Conclusions

An NPN SiGe GHBT structure with uniform 20 *at%* germanium in the base and tapering it linearly to zero *at%* Ge at the collector ohmic contact is proposed to improve the current gain performance of the SiGe HBTs at high collector current densities. The base-collector homojunction inhibits the formation of retarding potential barrier due to absence of valence band offset for holes at base-collector metallurgical junction and 20 *at%* of germanium and its tapering ensures the strained behavior and stability of the SiGe layers. The absence of retarding potential barrier in SiGe GHBT is observed to provide better current gain performance at high collector current densities in comparison with DHBT structure. A theoretical model for SiGe DHBT has been developed to supplement the simulation results for current gain dependence on the physical parameters and device structure. A comparison of conduction band electron energy, net carrier concentration profile and dependence of collector current density on the base emitter voltage has been provided for the SiGe HBT structures. The theoretical formulation and the simulated results on the current gain performance establish the superiority of the GHBT structure in comparison with the DHBT device configuration at high collector current densities.

References

[1] A. Schuppen, “SiGe-HBTs for mobile communication”, *Solid State Electron.*, 43 (1999) 1373-1381.
[2] O.A. Hammadi, F.J. Al-Maliki and E.A. Al-Oubidy, “Photocatalytic Activity of Nitrogen-Doped Titanium Dioxide Nanostructures Synthesized by DC Reactive Magnetron Sputtering Technique”, Nonl. Opt. Quant. Opt., 51(1/2) (2019) 67-78.
[3] Z. Yu, P.E. Cottrell and R.W. Dutton, “Modeling and simulation of high-level injection behavior in double heterojunction bipolar transistors,” *IEEE Bipolar Circuits and Technology Meeting*, 8.5 (1990) 192-194.
[4] R.A. Ismail et al., “Full characterization at 904 nm of large area Si p-n junction photodetectors produced by LID technique”, Euro. Phys. J. Appl. Phys., 38 (2007) 197-201.
[5] R. People and J.C. Bean, “Calculation of critical layer thickness versus lattice mismatch for Ge_xSi_{1-x}/Si strained-layer heterostructure”, *Appl. Phys. Lett.*, 47(3) (1985) 322-324.
[6] Md.R Hashim, R.F Lever and P. Ashburn, “2D simulation of the effects of transient enhanced boron out-diffusion from base of SiGe HBT due to an extrinsic base implant”, *Solid State Electron.*, 43 (1999) 131-140.
[7] O.A. Hammadi, “Production of nanopowders from physical vapor deposited films on nonmetallic substrates by conjunctional freezing-assisted ultrasonic extraction method”, Proc IMechE Part N: J Nanomater. Nanoeng. Nanosys., 232(4) (2018) 135-140.
[8] D.J. Roulston, **“Bipolar Semiconductor Devices”**, McGraw-Hill (NY, 1990).
[9] W.N. Raja et al., “Magnetic Field Distribution of Closed-Field Unbalanced Dual Magnetrons Employed in Plasma Sputtering Systems”, Iraqi J. Appl. Phys., 12(3) (2016) 35-42.

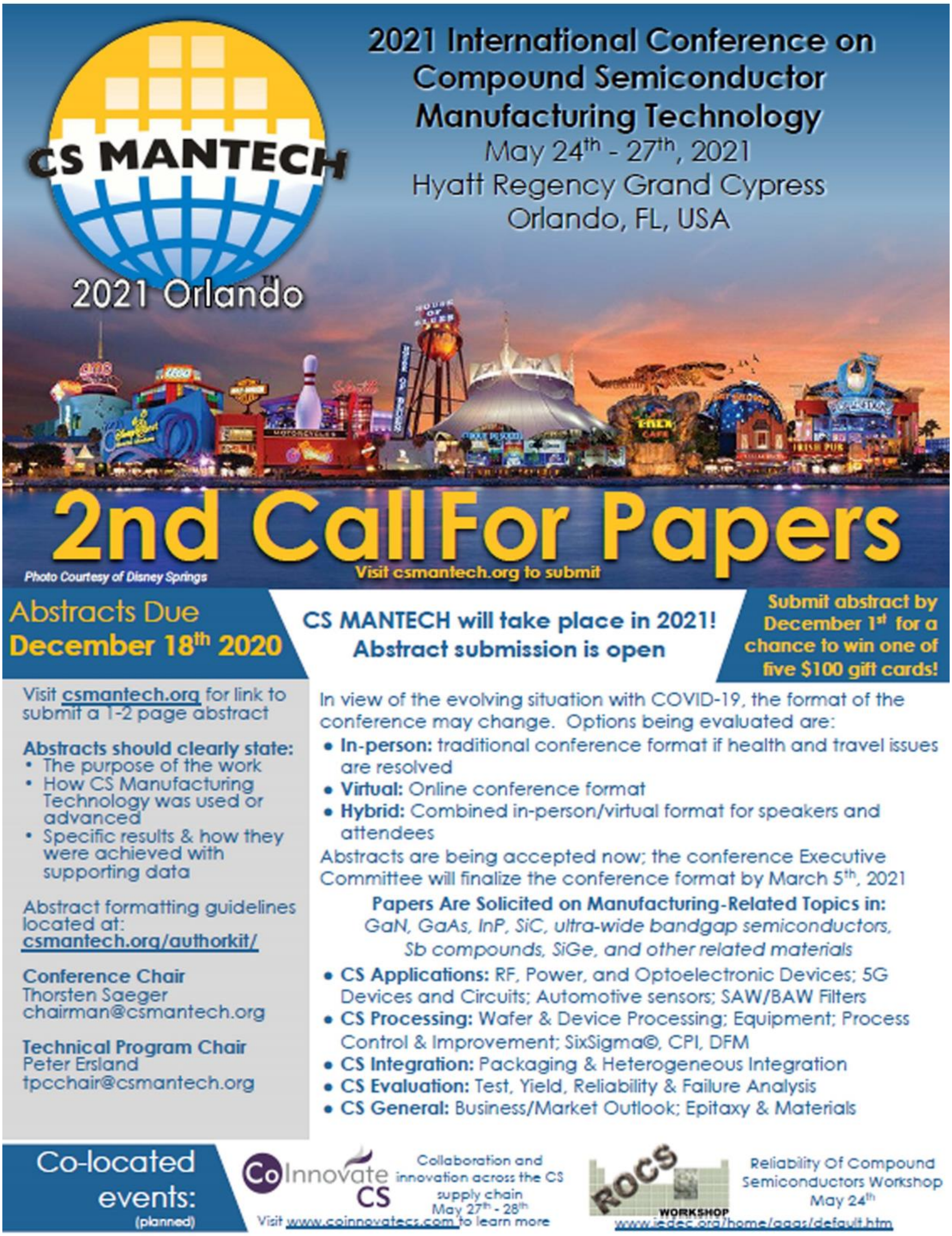
CS MANTECH
2021 Orlando
2021 International Conference on Compound Semiconductor Manufacturing Technology
May 24th - 27th, 2021
Hyatt Regency Grand Cypress
Orlando, FL, USA
2nd Call For Papers
Photo Courtesy of Disney Springs
Visit csmantech.org to submit
Abstracts Due
December 18th 2020
CS MANTECH will take place in 2021!
Abstract submission is open
Submit abstract by December 1st for a chance to win one of five $100 gift cards!
Visit csmantech.org for link to submit a 1-2 page abstract
Abstracts should clearly state:
• The purpose of the work
• How CS Manufacturing Technology was used or advanced
• Specific results & how they were achieved with supporting data
Abstract formatting guidelines located at: csmantech.org/authorkit/
Conference Chair
Thorsten Saeger
chairman@csmantech.org
Technical Program Chair
Peter Ersland
tpcchair@csmantech.org
In view of the evolving situation with COVID-19, the format of the conference may change. Options being evaluated are:
• In-person: traditional conference format if health and travel issues are resolved
• Virtual: Online conference format
• Hybrid: Combined in-person/virtual format for speakers and attendees
Abstracts are being accepted now; the conference Executive Committee will finalize the conference format by March 5th, 2021
Papers Are Solicited on Manufacturing-Related Topics in:
GaN, GaAs, InP, SiC, ultra-wide bandgap semiconductors, Sb compounds, SiGe, and other related materials
• CS Applications: RF, Power, and Optoelectronic Devices; 5G Devices and Circuits; Automotive sensors; SAW/BAW Filters
• CS Processing: Wafer & Device Processing; Equipment; Process Control & Improvement; SixSigma©, CPI, DFM
• CS Integration: Packaging & Heterogeneous Integration
• CS Evaluation: Test, Yield, Reliability & Failure Analysis
• CS General: Business/Market Outlook; Epitaxy & Materials
Co-located events:
(planned)
CoInnovate CS
Collaboration and innovation across the CS supply chain
May 27th - 28th
Visit www.coinnovatecs.com to learn more
ROCS WORKSHOP
Reliability Of Compound Semiconductors Workshop
May 24th
www.jedec.org/home/gaas/default.htm

IRAQI JOURNAL OF APPLIED PHYSICS
Vol. 16, No. 4, October-December 2020, pp. 25-30

Mohammed A. Hameed
Saja H. Faisal
Reem H. Turki

Department of Physics,
College of Science,
University of Baghdad,
Baghdad, IRAQ

Characterization of Multilayer Highly-Pure Metal Oxide Structures Prepared by DC Reactive Magnetron Sputtering Technique

In this work, multilayer nanostructures were prepared from two metal oxide thin films by dc reactive magnetron sputtering technique. These metal oxide were nickel oxide (NiO) and titanium dioxide (TiO_2). The prepared nanostructures showed high structural purity as confirmed by the spectroscopic and structural characterization tests, mainly FTIR, XRD and EDX. This feature may be attributed to the fine control of operation parameters of dc reactive magnetron sputtering system as well as the preparation conditions using the same system. The nanostructures prepared in this work can be successfully used for the fabrication of nanodevices for photonics and optoelectronics requiring highly-pure nanomaterials.

Keywords: Magnetron sputtering; Reactive sputtering; Multilayer structures; Nanostructures
Received: 21 November 2020; **Revised:** 22 December 2020; **Accepted:** 29 December 2020

1. Introduction

Several decades ago, the multilayer structures have attracted the research interests due to their advantages and features for both research and industrial purposes. These structures have mostly presented a mixture of advantages of all constituents included in the multilayer structure. However, they may show new features and characteristics not observed for the constituents individually [1-4]. This can be reasonably observed in spectroscopic studies as the multilayer structures can exhibit absorption higher than the individual absorption characteristics of their constituents in addition to new absorption peaks or edges in the regions of weak absorption [1].

Drastic developments were seen in the physics and technology of photonics and optoelectronics devices such as photodetectors, solar cells, gas sensors, photocatalysts, etc. [5-9]. Such devices represent the skeleton of the modern technologies, therefore, the research works are intensively focused on development and enhancement of their characteristics and performances [1,3,10]. Recently, nanotechnology has added more routes to develop them with new properties and characteristics [4].

Thin film deposition techniques made it easy to fabricate multilayer structures by consequent deposition of layers from different materials but most of these techniques may include a chemical reaction or physical changes in the properties of the lower layer when a new layer of different materials is deposited upon [3]. This problem may have negative effects on the outcome expected from a multilayer structure. Among all physical vapor deposition (PVD) methods and techniques, the reactive magnetron sputtering shows very good features in fabrication multilayer structures as no reactions that may change the properties of the lower layers are included [11,12]. As well, no mechanical or thermal processes exist to affect negatively the grown layers [13,14]. Therefore, high-quality multilayer structures can be successfully fabricated by reactive magnetron sputtering in addition to the advantages of low-cost large-scale production, reliability and reproducibility [15-18].

In this work, multilayer structures were fabricated from nickel oxide and titanium dioxide thin films prepared by dc reactive magnetron sputtering technique. The structural characteristics of the fabricated structures were introduced and analyzed.

2. Experiment

Highly-pure sheets of titanium (99.99%) and nickel (99.99%) were used as sputtering targets. The target was maintained inside the deposition chamber on the cathode. Pure oxygen was used as reactive gas required to form the metal oxides. The quartz substrates on which the metal oxide thin films are to be deposited were carefully cleaned and then put on the surface of the anode. The temperature of the anode (and the substrate as well) could be controlled and a thermocouple was used to measure it. More details on the magnetron sputtering system used in this work and shown in Fig. (1) can be found elsewhere [19-23].

Fig. (1) A photograph of the dc reactive magnetron sputtering system used in this work

The deposition chamber was first evacuated down to 10^{-3} mbar before filled with the gas mixture of argon and oxygen at a pressure of 0.1 mbar. The plasma required for sputtering was generated by the electric discharge of argon. Electrical power was provided by a high-voltage dc power supply. Several parameters of sputtering system, such as inter-electrode distance, deposition time, substrate temperature, total gas pressure and Ar:O_2 ratio, could be varied to determine their effects on the deposition process.

The fabricated multilayer structures were characterized by the Fourier-transform infrared (FTIR) spectroscopy, x-ray diffraction (XRD), scanning electron microscopy (SEM), energy-dispersive x-ray spectroscopy (EDX) and atomic force microscopy (AFM).

3. Results and Discussion

Figure (2) shows the FTIR spectrum of the multilayer sample prepared using Ar:O_2 gas mixture of 1:1 after deposition time of two hours. All peaks assigned for the vibration bands of M-O bonds were seen as shown in table (1). These bonds are distinctly recognized as both materials are metal oxide (NiO and TiO_2). The band assigned at 1064 cm^{-1} is ascribed to the vibration of the Ni-O bond [24] while three bands are observed for the TiO_2 sample at 409, 447 and 667 cm^{-1}, which ascribed to the vibration modes of the triatomic molecule (TiO_2) in addition to the peak assigned at 709 cm^{-1}, which is ascribed to the bridging stretching mode of Ti-O-Ti [25]. No bands ascribed to compounds other than O-H were observed, which confirms the structural purity of both types of samples (NiO and TiO_2) [26]. However, the O-H bands are unavoidable due to the adsorption of water from the environment. When compared to the individual FTIR spectra of NiO and TiO_2 samples prepared by the same technique, it is confirmed that no other phases were formed (e.g., Ni_2O_3, NiO_2, TiO or Ti_2O_3) nor new compound, such $NiTiO_3$ [27]. This is significant evidence for the advantage of reactive magnetron sputtering in fabrication of highly-pure multilayer structures.

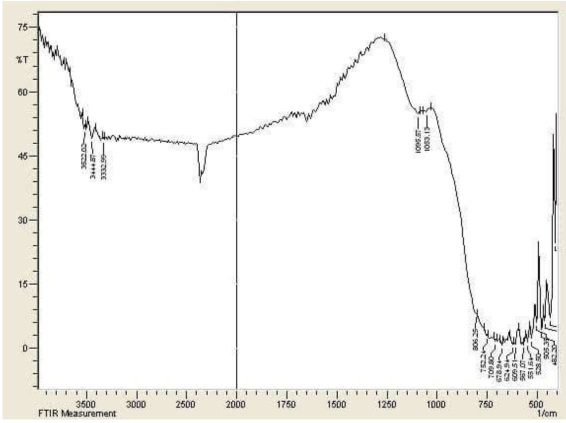

Fig. (3) The FTIR spectrum of the multilayer NiO/TiO_2 structure prepared in this work using 1:1 gas mixture after deposition time of 2 hours

Table (1) Vibration bands observed on the FTIR spectrum of the fabricated multilayer structure

Wavenumber (cm^{-1})	Assigned bond	Material
409	Ti-O-Ti	Bending
447	Ti-O	Symmetric stretching
667	Ti-O	Asymmetric stretching
709	Ti-O-Ti	Bridging
1064	Ni-O	Stretching

Figure (3) shows the XRD pattern of the multilayer structure prepared in this work using Ar:O_2 gas mixture of 1:1 after deposition time of two hours. As seen, two sharp and intensive peaks are observed at 2θ of 35.22° and 38.46°, which corresponding to the crystal planes of (111) and (200), respectively, of NiO. The peak assigned at 62.52° is belonging to the (220) crystal plane of NiO as well. Other lower peaks are all belonging to crystal planes TiO_2 [28-30]. As previously confirmed by the FTIR result, no peaks corresponding to reflection from crystal planes belonging to other compounds were observed. Table (2) shows the calculations of grain size based on the XRD results.

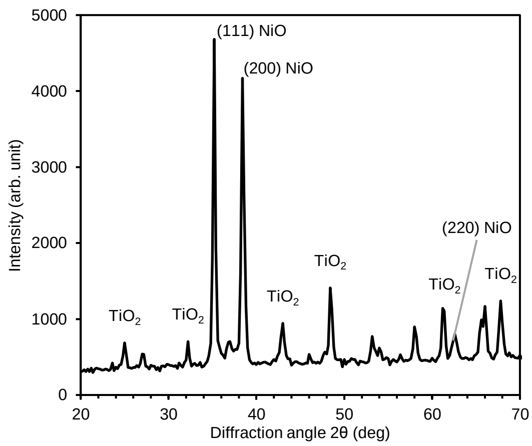

Fig. (2) XRD pattern of the NiO/TiO_2 multilayer structure prepared in this work using 1:1 gas mixture after deposition time of 2 hours

Table (2) Calculations of grain size based on the XRD results

2θ	d (Å)	D (nm)	Material
25.0162	3.55669	15.413	TiO_2
32.2164	2.77633	13.483	TiO_2
35.2254	2.54576	12.410	NiO
36.8363	2.43805	8.231	TiO_2
38.4639	2.33854	10.469	NiO
42.9806	2.10267	8.112	TiO_2
48.4665	1.87671	8.667	TiO_2
53.2587	1.71859	6.964	TiO_2
58.0355	1.58798	7.060	TiO_2
61.2700	1.51168	7.005	TiO_2
62.5275	1.48426	4.709	NiO
65.7933	1.41827	3.635	TiO_2
67.7970	1.38115	5.696	TiO_2

The formation of nanostructures in the prepared samples was identified by the SEM results as shown in Fig. (4). A minimum particle size of about 40 nm can be seen while no large aggregation is observed. As compared to the SEM results of NiO and TiO_2 samples individually, the surface morphology of the multilayer sample is similar to that of the TiO_2 sample. This can be attributed to the larger particle size of TiO_2 particles as the NiO nanoparticles of lower sizes are deposited on the vacancies among the larger particles. The spherical shape of NiO nanoparticles seen in Fig. (3a) approximately disappeared in the multilayer sample. Instead, larger particles appear with a possibility to be a combination of NiO nanoparticles attached to TiO_2 nanoparticles. If this is the situation, then the assumption of formation of nano-heterojunctions can be reasonably possible. Such assumption encourages to synthesize nanophotonics and nano-devices based on the optoelectronic characteristics of such heterojunctions.

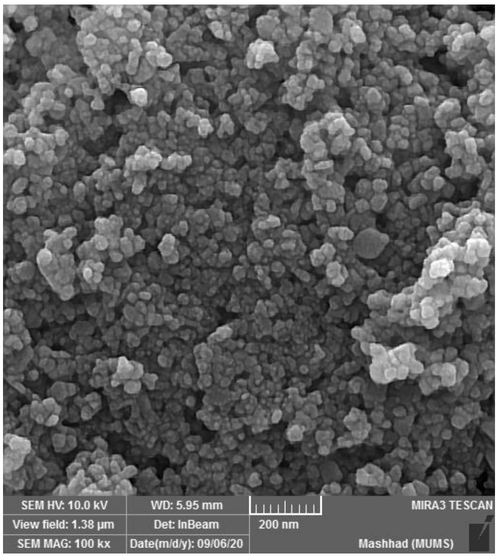

(a)

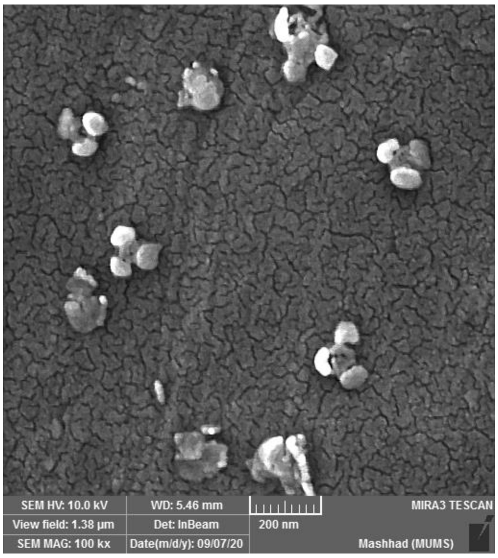

(b)

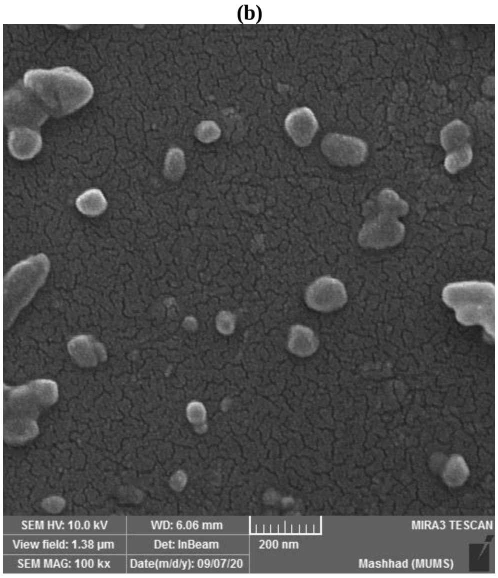

(c)

Fig. (3) The SEM image of the NiO sample (a), TiO2 sample (b) and multilayer NiO/TiO_2 structure (c) prepared in this work using 1:1 gas mixture after deposition time of 2 hours

With assumption of forming nano-heterojunctions from NiO and TiO_2 nanoparticles, and considering the concentrations of solid species that may reach up to 10^{18} cm^{-3}, the formation of up to 10^{12} nano-heterojunctions is very likely. When compared to conventional thin film structures (NiO/TiO_2), these multilayer structures are much more efficient by about 1000%. Therefore, the tiny contributions of such nano-devices can produce a huge amount of outcome (energy, current, voltage, etc.). Accordingly, a drastic development in their applications can be expected with further control of the nanoparticle size and distribution [31-35].

The elemental constitution of each sample (NiO and TiO_2) as well as the fabricated multilayer structure was individually characterized by EDX, as shown in Fig. (4). Both structures can be considered highly pure as no traces for other elements other than Ni, Ti and O were seen. In addition, the multilayer structure has confirmed that its formation processes did not include any opportunity for other elements to be exist in the final sample as dopants or contaminants. This result additionally supports the advantage of reactive magnetron sputtering technique in production of highly-pure nanostructures.

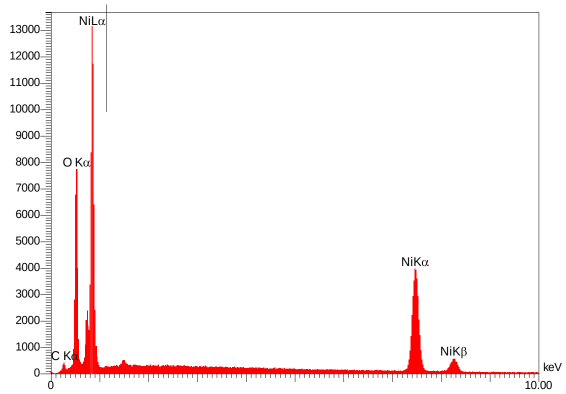

(a)

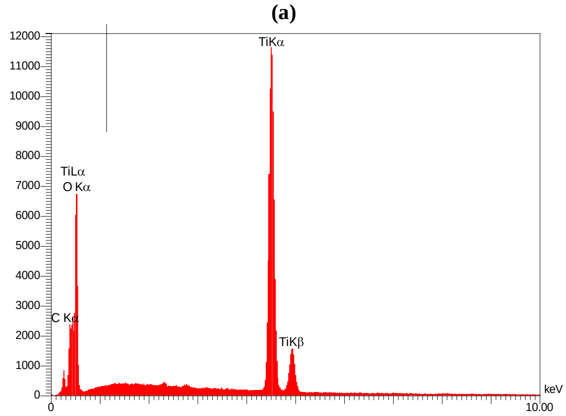

(b)

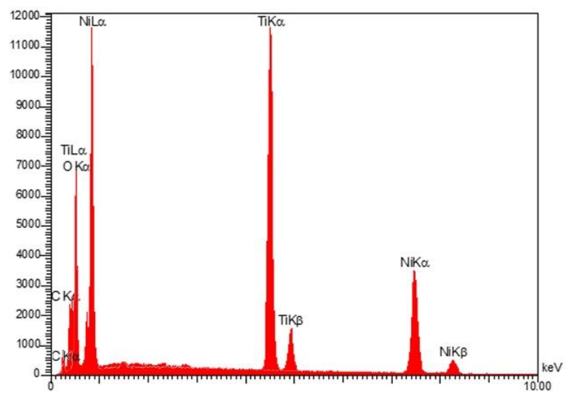

(c)

Fig. (4) Results of EDX of the NiO (a), TiO_2 (b) and multilayer (c) samples prepared in this work using 1:1 gas mixture after deposition time of 2 hours

Multilayer structures – like those fabricated in this work – can be successfully employed in photonics, optoelectronics, spectroscopic and other applications including an interaction between the electromagnetic radiation and matter. As well, gas sensors for more than one gas can be fabricated from such structures [36,37]. Therefore, the surface roughness is an important parameters to make such interaction much more efficient. The topography of the synthesized multilayer structures was introduced by the AFM as shown in Fig. (5) showing the 2D and 3D images of their surfaces. The average roughness was determined to be 16.7 nm while the root-mean-square roughness was about 19.5 nm. These surfaces can also be considered highly homogeneous with a surface skewness of about 0.0224. It is known that lower values of surface skewness correspond to rougher surfaces while higher values (up to ∞) correspond to smoother surfaces [?]. These values reflect the high surface area that can be available for the interaction between these nano-surfaces and electromagnetic radiation or gas species to be sensed.

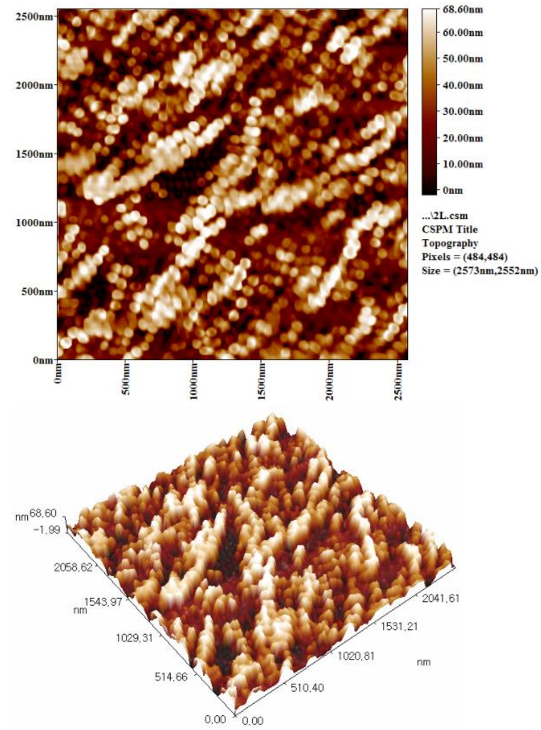

Fig. (5) The 2D and 3D AFM images of the multilayer NiO/TiO_2 structure prepared in this work using 1:1 gas mixture after deposition time of 2 hours

4. Conclusion

In concluding remarks, the fabrication and characterization of multilayer nanostructures from NiO and TiO_2 by dc reactive magnetron sputtering technique were presented. These nanostructures showed high structural purity with no imperfections or degradation when compared to the nanostructures of NiO and TiO_2 individually as well as to the thin film NiO/TiO_2 structures. These results encourage to employ such multilayer structures in many photonics and optoelectronics applications due to their advantages as low-cost highly-pure nano-surfaces.

References

[1] M. Ohring, **"The Materials Science of Thin Films"**, Academic Press (London, 1992), p. 310.

[2] E. Kaxiras, **“Atomic and Electronic Structure of Solids”**, Cambridge University Press (NY, 2003), p. 342.
[3] B. Bhushan, **“Springer Handbook of Nanotechnology”**, Springer-Verlag (Berlin, 2004), p. 1.
[4] B.S.R. Reddy, **“Advances in Diverse Industrial Applications of Nanocomposites”**, InTech (2011), p. 57.
[5] W.A. Goddard et al., **“Handbook of Nanoscience, Engineering and Tehnology”**, CRC Press (FL, 2003), p. 65
[6] O.A. Hamadi, B.A.M. Bader and A.K. Yousif, “Electrical Characteristics of Silicon p-n Junction Solar Cells Produced by Plasma-Assisted Matrix Etching Technique”, Eng. Technol. J., 28 (2008) 995-1001.
[7] A.A.K. Hadi and O.A. Hamadi, “Optoelectronic Characteristics of As-doped Silicon Photodetectors Produced by LID Technique”, Iraqi J. Appl. Phys. Lett., 1(2) (2008) 23-26.
[8] A.J. Mohammad, A.M. Mousa and K.H. Hussain, “Optical and Electrical Properties of ZnO Thin Films Prepared by Spray Pyrolysis Technique”, Iraqi J. Appl. Phys., 4(1) (2008) 31-35.
[9] A.K. Yousif and O.A. Hamadi, “Plasma-Induced Etching of Silicon Surfaces”, Bulg. J. Phys., 35(3) (2008) 191-197.
[10] E.A. Al-Oubidy and F.J. Al-Maliki, “Effect of Gas Mixing Ratio on Energy Band Gap of Mixed-Phase Titanium Dioxide Nanostructures Prepared by Reactive Magnetron Sputtering Technique”, Iraqi J. Appl. Phys., 14(4), 19-23 (2018).
[11] O.A. Hamadi, “Effect of Annealing on the Electrical Characteristics of CdO-Si Heterostructure Produced by Plasma-Induced Bonding Technique”, Iraqi J. Appl. Phys., 4(3) (2008) 34-37.
[12] G.H. Mohammed, “Characterization of $(CdO)_{1-x}(ZnO)_x$ Thin Films Prepared by Pulsed-Laser Deposition for Solar Cell Applications”, Iraqi J. Appl. Phys., 11(3) (2015) 3-7.
[13] O.A. Hammadi and N.E. Naji, “Electrical and Spectral Characterization of CdS/Si Heterojunction Prepared by Plasma-Induced Bonding”, Opt. Quant. Electron., 48(8) (2016) 375.
[14] G.M.A. Youssef, A.M.H. El-Naggar and A.S. Megazy, “Characterization of E-Mode InZnO Thin Film Transistors Produced by DC Sputtering Technique”, Iraqi J. Appl. Phys. Lett., L3(1) (2008) 19-22.
[15] O.A. Hamadi and K.Z. Yahiya, “Optical and electrical properties of selenium-antimony heterojunction formed on silicon substrate”, Sharjah Univ. J. Pure Appl. Sci. (UoS J PAS), 4(2) (2007) 1-11.
[16] H. Afifi, M. Abdel-Naby, S. El-Hefnawie, A. Eliewa and N. Ahmad, “Optical and Electrical Properties of Zinc Oxide Films Prepared by Spray Pyrolysis”, Iraqi J. Appl. Phys., 6(4) (2006) 23-28.
[17] O.A. Hamadi, “Characteristics of CdO-Si Heterostructure Produced by Plasma-Induced Bonding Technique”, Proc. IMechE, Part L, J. Mater.: Design and Applications, 222 (2008) 65-71.
[18] J. Cheng et al., “Recent Advances in Optoelectronic Devices Based on 2D Materials and Their Heterostructures”, Adv. Opt. Mater., 7(1) (2019) 1800441.
[19] O.A. Hammadi, M.K. Khalaf, F.J. Kadhim, B.T. Chiad, “Operation Characteristics of a Closed-Field Unbalanced Dual-Magnetrons Plasma Sputtering System”, Bulg. J. Phys., 41(1) (2014) 24-33.
[20] O.A. Hammadi, W.N. Raja, M.A. Saleh and W.A. Altun, “Employment of Magnetron to Enhance Langmuir Probe Characteristics of Argon Glow Discharge Plasma in Sputtering System”, Iraqi J. Appl. Phys., 12(4) (2016) 19-28.
[21] O.A. Hammadi, M.K. Khalaf, F.J. Kadhim, “Fabrication and Characterization of UV Photodetectors Based on Silicon Nitride Nanostructures Prepared by Magnetron Sputtering”, Proc. IMechE, Part N, J. Nanoeng. Nanosys., 230(1) (2016) 32-36.
[22] M.A. Hameed and Z.M. Jabbar, “Optimization of Preparation Conditions to Control Structural Characteristics of Silicon Dioxide Nanostructures Prepared by Magnetron Plasma Sputtering”, Silicon, 10(4) (2018) 1411-1418.
[23] F.J. Al-Maliki and E.A. Al-Oubidy, “Effect of gas mixing ratio on structural characteristics of titanium dioxide nanostructures synthesized by DC reactive magnetron sputtering”, Physica B: Cond. Matter, 555, 18-20 (2019).
[24] N.N. Greenwood and E.J.F. Ross, **“Index of Vibrational Spectra of Inorganic and Organometallic Compounds”**, vol. I, Butterworth Group (London), p. 326, 328 (1960).
[25] N.N. Greenwood and E.J.F. Ross, **“Index of Vibrational Spectra of Inorganic and Organometallic Compounds”**, vol. II, Butterworth Group (London), p. 457 (1963).
[26] N.N. Greenwood and E.J.F. Ross, **“Index of Vibrational Spectra of Inorganic and Organometallic Compounds”**, vol. III, Butterworth Group (London), p. 800, 1078 (1966).
[27] V.P. Tolstoy, I.V. Chernyshova and V.A. Skryshevsky, **“Handbook of Infrared Spectroscopy of Ultrathin Films”**, John Wiley & Sons, Inc. (NJ), p. 435 (2003).

[28] F.J. Al-Maliki, O.A. Hammadi and E.A. Al-Oubidy, "Optimization of Rutile/Anatase Ratio in Titanium Dioxide Nanostructures prepared by DC Magnetron Sputtering Technique", Iraqi J. Sci., 60 (Special Issue), 91-98 (2019).
[29] S.H. Faisal and M.H. Hameed, "Heterojunction Solar Cell Based on Highly-Pure Nanopowders Prepared by DC Reactive Magnetron Sputtering", Iraqi J. Appl. Phys., 16(3) (2020) 27-32.
[30] R.H. Turki and M.H. Hameed, "Spectral and Electrical Characteristics of Nanostructured NiO/TiO_2 Heterojunction Fabricated by DC Reactive Magnetron Sputtering", Iraqi J. Appl. Phys., 16(3) (2020) 39-42.
[31] O.A. Hammadi, "Effects of Extraction Parameters on Particle Size of Titanium Dioxide Nanopowders Prepared by Physical Vapor Deposition Technique", Plasmonics, 15 (2020),DOI: 10.1007/s11468-020-01205-8
[32] O.A. Hammadi, "Photovoltaic Properties of Thermally-Grown Selenium-Doped Silicon Photodiodes for Infrared Detection Applications", Photon. Sens., 5(2) (2015) 152-158.
[33] O.A. Hammadi, "Production of Nanopowders from Physical Vapor Deposited Films on Nonmetallic Substrates by Conjunctional Freezing-Assisted Ultrasonic Extraction Method", Proc. IMechE, Part N, J. Nanomater. Nanoeng. Nanosys., 232(4), 135-140 (2018).
[34] O.A. Hammadi, M.K. Khalaf, F.J. Kadhim, "Fabrication of UV Photodetector from Nickel Oxide Nanoparticles Deposited on Silicon Substrate by Closed-Field Unbalanced Dual Magnetron Sputtering Techniques", Opt. Quantum Electron., 47(12) (2015) 3805-3813.
[35] O.A. Hammadi, M.K. Khalaf, F.J. Kadhim, "Silicon Nitride Nanostructures Prepared by Reactive Sputtering Using Closed-Field Unbalanced Dual Magnetrons", Proc. IMechE, Part L, J. Mater.: Design and Applications, 231(5) (2017) 479-485.
[36] R.A. Ismail, O.A. Abdulrazaq, A.A. Hadi and O.A. Hamadi, "Characterization of Si p-n Photodetectors Produced by Laser-Induced Diffusion", Int. J. Mod. Phys., 19(31) (2005) 4619-4628.
[37] R.A. Ismail, O.A. Abdulrazaq, A.A. Hadi and O.A. Hamadi, "Full Characterization at 904nm of Si p-n Junction Photodetectors Produced by LID Technique", Euro. Phys. J.: Appl. Phys., 38 (2007) 197-201.
[38] W.K. Khalef, A.A. Aljubouri and H.G. Rashid, "Zinc Oxide Nanowires Prepared by Oblique Angle Deposition Method", Iraqi J. Appl. Phys., 12(1) (2016) 3-7.
[39] F.K. Fuss, "The effect of surface skewness on the super/postcritical coefficient of drag of roughened cylinders", Procedia Eng., 13 (2011) 284-289.

Iraqi Journal of Applied Physics

P. O. Box 55259, Baghdad 12001, IRAQ
www.iraqiphysicsjournal.com
Email: info@iraqiphysicsjournal.com
Email: editor_ijap@yahoo.co.uk
Email: irq_appl_phys@yahoo.com

Subject Index 2005-2020

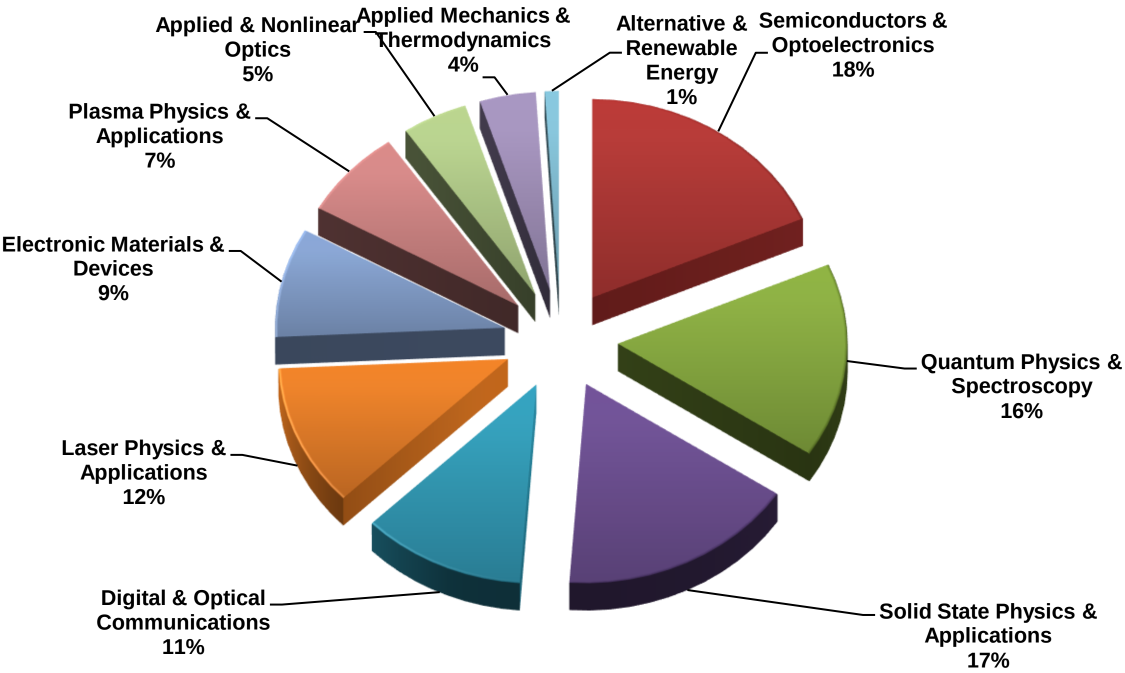

Alternative & Renewable Energy

IJAP-AARE

Applied & Nonlinear Optics

IJAP-AANO

Applied Mechanics & Thermodynamics
IJAP-AMAT

Digital & Optical Communications
IJAP-DAOC

Electronic Materials & Devices
IJAP-EMAD

Laser Physics & Applications
IJAP-LPAA

Plasma Physics & Applications
IJAP-PPAA

Quantum Physics & Spectroscopy
IJAP-QPAS

Semiconductors & Optoelectronics
IJAP-SCAOE

Solid State Physics & Applications
IJAP-SSPAA

* * *

Notes:

- 1(1), 3 refer to IJAP, Vol. 1, No. 1, page 3
- L1(1), 3 refer to IJAPLett, Vol. 1, No. 1, page 3

IRAQI JOURNAL OF APPLIED PHYSICS
IJAP, Vol. 16, No. 4, October-December 2020, pp. 37-42

Iraqi Journal of Applied Physics

P. O. Box 55259, Baghdad 12001, IRAQ
www.iraqiphysicsjournal.com
Email: info@iraqiphysicsjournal.com
Email: editor_ijap@yahoo.co.uk
Email: irq_appl_phys@yahoo.com

Author Index 2005-2020

 ISSN (printed) 1813-2065, (online) 2309-1673

B

C

D

E

F

G

THE IRAQI JOURNAL OF APPLIED PHYSICS
EDITORIAL BOARD

COPYRIGHT RELEASE FORM
IRAQI JOURNAL OF APPLIED PHYSICS (IJAP)

We, the undersigned, the author/authors of the article titled

………
………
………
………
………
………
………

that is submitted to the Iraqi Journal of Applied Physics (IJAP) for publication, declare that we have neither taken part or full text from any published work by others, nor presented or published it elsewhere in any other journal. We also declare transferring copyrights and conduct of this article to the Iraqi Journal of Applied Physics (IJAP) after accepting it for publication.

The authors will keep the following rights:
1. Possession of the article such as patent rights.
2. Free of charge use of the article or part of it in any future work by the authors such as books and lecture notes after informing IJAP editorial board.
3. Republishing the article for any personal purposes of the authors after taking journal permission.

To be signed by all authors:

Signature:……………………………………………………….…..date: ……………………….…………………
Printed name: ………

Signature:……………………………………………………….…..date: ……………………….…………………
Printed name: ………

Signature:……………………………………………………….…..date: ……………………….…………………
Printed name: ………

Correspondence
address:……………………..………………………………………………………………………...
……
Address:……………………………………………………..………………………………………………
……
Telephone:…………………………..…………………….email: ………………………………………………………

Note: Complete and sign this form and mail it to the below address with your finally revised manuscript

The Iraqi Journal of Applied Physics
www.iraqiphysicsjournal.com
Email: info@iraqiphysicsjournal.com
Email: editor_ijap@yahoo.co.uk
Email: irq_appl_phys@yahoo.com

IRAQI JOURNAL OF APPLIED PHYSICS
Volume (16), Issue (4), October-December 2020

CONTENTS